The effect of co-amorphization of glibenclamide on its dissolution properties and permeability through an MDCKII-MDR1 cell layer

Henri Sormunen[a], Marika Ruponen[a], Riikka Laitinen[a*]

[a] School of Pharmacy, University of Eastern Finland, P.O.Box 1627, 70211, Kuopio, Finland

*Corresponding author:

Riikka Laitinen

School of Pharmacy

University of Eastern Finland

P.O.Box 1627

70211 Kuopio

FINLAND

Phone:+358 50 5695 303

e-mail: riikka.laitinen@uef.fi

Abstract

Co-amorphous mixtures have been demonstrated to represent a promising approach for enhancing the dissolution of poorly water-soluble drugs. However, little is known of their permeability properties, especially through biological membranes, or about the relationship between their dissolution and permeability. In the present study, co-amorphous glibenclamide (GBC) mixtures with two amino acids, arginine (ARG) and serine (SER), in molar ratios of 1:1 were prepared by cryomilling. Their dissolution and permeability properties were studied in side-by-side diffusion chambers using cell layers containing Madine Darby kidney cells overexpressing P-glycoprotein (Pgp) transporters (MDCKII-MDR1), as Pgp may influence the absorption of GBC. Furthermore, two other compounds, the flavonoid quercetin (QRT) which is a Pgp inhibitor and the surfactant, sodium lauryl sulfate (SLS), were used as excipients to investigate if they improved either passive or active diffusion of GBC. In addition, amorphous QRT and a co-amorphous mixture of GBC and QRT (1:1) were characterized with respect to their solid-state properties and physical stability.

It was demonstrated that co-amorphous GBC mixtures exhibited superior dissolution properties over the corresponding physical mixtures and amorphous GBC. Furthermore, the co-amorphous GBC-ARG-SLS mixture exhibited a 9-fold increase in permeating through the MDCKII-MDR1 cell layer as compared to the corresponding physical mixture. There was a correlation between the dissolution and permeability area under curve (AUC) values, evidence that the main mechanism behind the improved permeability of co-amorphous mixtures was their improved dissolution. The simultaneous dissolution/permeation testing with side-by-side diffusion chambers and MDCKII-MDR1 cells proved to be a feasible method for evaluating the dissolution/permeation interplay of amorphous compounds.

Keywords: Amino acid; co-amorphous; dissolution; MDCKII-MDR1; permeability; stability

Abbreviations[1]

[1] AA, amino acid; ACN, acetonitrile; ARG, arginine; AUC, area under curve; BCS, biopharmaceutical classification system; CM, cryomilling; DMEM, Dulbecco's modified eagle medium; DS, degree of supersaturation; DSC, differential scanning calorimetry; FBS, fetal bovine serum; FTIR, fourier transform infrared spectroscopy; GBC, glibenclamide; HPLC, high performance liquid chromatography; PBS, phosphate buffered saline; Pgp, p-glycoprotein; PM, physical mixture; QRT, quercetin; SD, solid dispersion; SER, serine; T_g, glass transition temperature; T_m, melting point; TEER, transepithelial electrical resistance; XRPD, X-ray powder diffraction

1. Introduction

An increasing number of drugs in the development pipeline encounter problems with aqueous solubility (Hauss, 2007; Lipinski et al., 2001). Oral administration is the preferred route due to ease of manufacture of the dosage form (tablets) and good compliance by patients, but it may be difficult to develop oral dosage forms of drugs with poor solubility and dissolution properties (Williams et al., 2013). Hence, there is a growing need for techniques that can enhance the dissolution of Biopharmaceutical classification system (BCS) class II and IV drugs with inadequate solubility properties.

One widely used strategy to improve the dissolution of the poorly soluble drugs is to modify their solid-state structures into amorphous forms (Laitinen et al., 2017). Due to its thermodynamic instability, an amorphous material has improved apparent solubility, known as “the spring effect”, in comparison to their crystalline counterparts (Brouwers et al., 2009). However, due to their high internal energy, stability can be a commonly encountered problem with amorphous materials. Recently, a promising approach has been presented which involves the combination of a poorly soluble drug with low molecular weight components, such as amino acids or drug molecules, i.e. creating a co-amorphous formulation (Allesø et al., 2009; Löbmann et al., 2011; Löbmann et al., 2013a; Löbmann et al., 2013b). These co-amorphous mixtures are homogeneous single-phase systems in which the components are mixed with each other (Löbmann et al., 2011). In addition to the improved physical stability, co-amorphous formulations possess enhanced dissolution rates and supersaturated states in comparison with either individual crystalline or amorphous drugs (Beyer et al., 2017; Dengale et al., 2016; Heikkinen et al., 2015; Jensen et al., 2015; Kasten et al., 2017; Löbmann et al., 2012).

Despite the superior dissolution profiles of co-amorphous mixtures, their permeability properties i.e. their abilities to cross (biological) membranes, have remained virtually unexplored. Previously different experimental setups have been used, such as chambers separated by both artificial membranes and/or cell layers, to study the permeability of individual drugs (Kataoka et al., 2014; Sironi

et al., 2017). At present, the permeability of co-amorphous mixtures has been examined using parallel artificial membrane permeability assay (PAMPA) membranes (Mesallati et al., 2017), but this experimental setup did not explore the effect of drug dissolution rate and supersaturation, as fixed concentrations were used in the donor compartment. Recently, side-by-side diffusion chambers separated by a PAMPA layer were demonstrated to be a feasible method for evaluating simultaneously dissolution and permeability of amorphous products (Ruponen et al., 2018). However, further investigation of the effect of co-amorphization on permeability through biological membranes is needed, as the role of active diffusion has remained unexplored.

The aim of this study was to gain a deeper insight into the relationship between dissolution and permeability through a cellular layer for co-amorphous mixtures. A BCS class II drug glibenclamide (GBC) was used as a model drug, for which poor solubility and dissolution are factors limiting its bioavailability. In a recent study, we demonstrated that co-amorphization of GBC with arginine (ARG), serine (SER) and sodium lauryl sulfate (SLS) enhanced the drug's dissolution and permeability through a PAMPA membrane (Ruponen et al., 2018). In that study, co-amorphous GBC-ARG and GBC-ARG-SLS mixtures displayed superior dissolution properties (due to possible salt formation between GBC and ARG) promoting the flux of GBC through the PAMPA membrane. In the case of GBC, it was evident that further investigation of the role of P-glycoprotein (Pgp) would be needed as it has been observed that Pgp may influence the absorption of GBC (Srirangam and Vidya Sagar, 2010). Thus, here we used side-by-side diffusion chambers to investigate simultaneously the dissolution and permeability of GBC through MDCKII (Madine Darby kidney cells) cell layer overexpressing Pgp using the above mentioned co-amorphous formulations which had been prepared by cryomilling. In addition, a Pgp-inhibitor quercetin (QRT) was also used as an excipient to investigate the possible role of efflux of GBC. The co-amorphous mixtures containing QRT (1:1 molar ratio) were also characterized using X-ray powder diffraction (XRPD), differential scanning calorimetry (DSC) and Fourier transform infrared spectroscopy (FTIR). In addition, we determined the physical stability of a co-amorphous GBC-QRT mixture under

accelerated storage conditions. To the best of our knowledge, this cell-based setup has not been previously used to study the permeability properties of a co-amorphous material.

2. Materials and methods

2.1 Materials

Glibenclamide (GBC, M = 494.003 g/mol, 99 % - 101 %, Hangzhou Dayangchem Co Ltd., Hangzhou, China) was used as the model drug in the study (Fig. 1). L-arginine (ARG, M = 174.2 g/mol, reagent grade, ≥ 98 %, Sigma-Aldrich, St. Louis, USA), L-serine (SER, M = 105.1 g/mol, 99 % - 101 %, Hangzhou Dayangchem Co Ltd., Hangzhou, China), quercetin (QRT, M= 302.24 g/mol, ≥ 95 % (HPLC), Sigma-Aldrich, St. Louis, USA) and sodium lauryl sulfate (SLS, M= 288.4, BioXtra, ≥ 99 %, Sigma-Aldrich, St. Louis, USA) were used as excipients in the co-amorphous mixtures (Fig. 1). Di-phosphorus pentoxide (P_2O_5, M= 141.95 g/mol, for analysis, Merck KGaA, Darmstadt, Germany) and a saturated solution of sodium bromide (NaBr) were used to maintain relative humidities (RH) of 0 % and 60 %, respectively. Madine Darby kidney cells overexpressing P-glycoprotein (Pgp) transporter (MDCKII-MDR1) were obtained from the Netherlands Cancer Institute (Amsterdam, Netherlands). Dulbecco´s modified Eagle medium (DMEM), fetal bovine serum (FBS), penicillin-streptomycin (10 000 U/ml) and phosphate-buffered saline (PBS) were from Gibco by Life Technologies Corporation (Thermo Fisher Scientific, Karlsruhe, Germany) and used for cell culturing. Hank's balanced salt solution (HBSS) (10X) and sodium bicarbonate solution 7.5 % both from Gibco by Life Technologies Corporation (Thermo Fisher Scientific, Karlsruhe, Germany) and HEPES (Bioperformance certified, ≥ 99.5 % (titration), cell culture tested, Sigma-Aldrich, St. Louis, USA) were used for preparing the HBSS pH 7.4 according to the manufacturer's protocol (Thermo Fisher Scientific: Preparing Salt Solutions from Powder concentrates, 2018). Mannitol D-[1-^{3}H(N)]-973.1 GBq/mmol (NEN Life Science Products, Boston, USA) and Ultima Gold® (PerkinElmer Inc., Waltham, USA) were used for radioactivity measurements. Acetonitrile (ACN) (HPLC grade, Fisher Scientific U.K. Limited, Loughborough, United Kingdom), trifluoroacetic acid (TFA) (CHROMANORM®, Sigma-Aldrich, St. Louis, USA) and class 1 water (Purelab Ultra, Elga Labwater, High Wycombe, United Kingdom) were used in the high performance liquid chromatography (HPLC) analysis.

2.2 Preparation of the co-amorphous mixtures

Powders for GBC-ARG, GBC-SER and GBC-QRT mixtures were weighed with an analytical balance (Sartorius analytic 200S, Sartorius Weighing Technology GmbH, Göttingen, Germany) in a molar ratio of 1:1, respectively, hence the total mass of each mixture was 500 mg. For GBC-ARG-SLS mixture, GBC and ARG were weighed in a molar ratio of 1:1 and 1 mg of SLS was added for every 10 mg of the 1:1 (n:n) mixture of GBC-ARG. Thus, the amount of SLS in the GBC-ARG-SLS mixture was equivalent of 9.09 % of the total mass of the mixture and it produced concentrations below the CMC of SLS in a side-by-side dissolution chamber.

The co-amorphous mixtures were prepared by cryomilling (CM) at 30 Hz and for 60 min in an oscillatory ball mill (Mixer Mill MM400, Retsch GmBH & Co., Haan, Germany). The weighed powder mixtures were transferred to 25 ml milling chambers with two 12 mm stainless steel balls. Prior to the cryomilling process, the chambers were cooled in liquid nitrogen for two min. At 10 min intervals during the milling process, the chambers were cooled for two min to prevent heating of the chambers. After 60 min of milling, the chambers were stored in a desiccator until they reached room temperature before opening to prevent moisture absorption. Subsequently, the samples were stored in a refrigerator (T=4 °C) in 0 % relative humidity (RH). RH 0 % was maintained with di-phosphorus pentoxide.

2.3 Characterization of co-amorphous mixtures

2.3.1 X-ray powder diffraction

In the X-ray powder diffraction (XRPD) analysis, a Bruker D8 DISCOVER system (Bruker AXS GmbH, Karlsruhe, Germany) with Cu Kα radiation with λ = 1.542 Å was used. Scanning of the samples was conducted with an acceleration voltage of 40 kV and a current of 40 mA from 5° to 35° 2 θ. A scanning speed of 0.12°/s and a step size of 0.013° were used.

2.3.2 Differential scanning calorimetry

For crystalline QRT, QRT CM and GBC-QRT CM differential scanning calorimetry (DSC) thermograms were obtained using Mettler Toledo DSC823 (Mettler Toledo, Schwerzenbach, Switzerland). DSC was equipped with an METT-FT900 Julabo intercooler (Mettler Toledo, Schwerzenbach, Switzerland) and a TS080IRO autosampler (Mettler Toledo, Schwerzenbach, Switzerland) and a nitrogen flow of 50 ml/min. The samples were weighed on an analytical balance (Sartorius SE2, Sartorius AG, Germany) on aluminum pans (Mettler Toledo, Schwerzenbach, Switzerland). Pans were sealed with pierced lids.

Crystalline QRT and QRT CM were analyzed between 25 °C and 350 °C at a heating rate of 10 °C/min. GBC-QRT CM samples were measured between 0 °C and 350 °C at a heating rate of 1 °C/min using temperature modulated DSC TOPEM® ± 0.25 K (Mettler Toledo, Schwerzenbach, Switzerland). STAR^e Evaluation Software (Mettler Toledo, Schwerzenbach, Switzerland) was used to determine the glass transition temperatures (T_g, midpoint) and possible recrystallization (T_{rc}, onset) and melting (T_m, onset). All samples were analyzed in duplicate from which averages and standard deviations were calculated.

The Gordon-Taylor equation was used to calculate a theoretical T_g value for the GBC-QRT mixture (Equation 1).

$$T_{g,mix} = \frac{w_1 \times T_{g1} + K \times w_2 \times T_{g2}}{w_1 + K \times w_2} \quad \text{(Equation 1)},$$

in which w_1 and w_2 are the mass ratios of the components in the mixture, T_{g1} and T_{g2} are the glass transition temperatures of the components (Kelvin, K) and K is a constant which was approximated with Simha-Boyer's rule (Equation 2):

$$K = \frac{\rho_1 \times T_{g1}}{\rho_2 \times T_{g2}} \quad \text{(Equation 2)},$$

in which ρ_1 and ρ_2 are the densities of the pure components (g/cm^3). The densities of ρ_{GBC}= 1.37747 g/cm^3 and ρ_{QRT} = 1.16606 g/cm^3 obtained from the Cambridge Structural Database were used for calculation of $T_{g,mix}$ (Byrn et al., 1986; Vasisht et al., 2016).

2.3.3 Fourier-transform infrared spectroscopy

The manufactured co-amorphous mixtures were characterized by using Thermo Nicolet Nexus 8700 Fourier-transform infrared spectroscopy (FTIR) spectrometer (Thermo Nicolet Nexus, Madison, Wisconsin, USA) with an Attenuated Total Reflectance (ATR) accessory. The spectra were recorded between 650–4000 cm^{-1}, with a resolution of 4 cm^{-1}, and 64 scans per sample were collected. OMNIC software (Thermo Nicolet Nexus, Madison, Wisconsin, USA) was used to collect the data.

2.4 Physical stability studies

The physical stabilities of GBC-QRT CM and QRT CM were studied at three storage conditions: 4 °C/0 % relative humidity (RH), room temperature/60 % RH and 40 °C/0 % RH. The samples were analyzed by XRPD on days 0, 10, 30, 60, 132 and at 13 months, and by FTIR on days 0, 60, 132 and at 13 months. Stability studies were continued until recrystallization was observed.

2.5 The equilibrium solubility of GBC in HBSS

The equilibrium solubilities of crystalline GBC and GBC in physical mixtures containing GBC-ARG, GBC-ARG-SLS, GBC-SER and GBC-QRT were determined. GBC and the physical mixtures were transferred to Erlenmeyer flasks containing 10 ml of HBSS solution. The flasks were kept in an OLS 200 water bath shaker (Grant Instruments (Cambridge) Ltd, Shepreth, United Kingdom) at T= 37 °C for 72 hours ensuring that during the test there were powders left in every flask. Samples were filtered through 0.45 µm Jet Biofil® (Guangzhou JET Bio-Filtration Co. Ltd, Guangzhou, China) syringe filters. The

samples were diluted with ACN (3/7 V/V) and a further dilution with a ACN/H_2O 70/30 –solution (1:4 V/V). A volume of 150 µl was pipetted into HPLC tubes and diluted with 350 µl of acetonitrile (ACN) and analyzed with an HPLC-UV method.

2.6 Dissolution studies

Dissolution studies were conducted in 3 ml side-by-side diffusion chambers (PermeGear Inc., Hellertown, USA). Water was conveyed to the water jackets of the chambers and heated to T=37 °C using a M3 Lauda water bath (Lauda Brinkmann, Königshofen, Germany) with an M5 Lauda thermostat (Lauda Brinkmann, Königshofen, Germany). Plastic cards were placed as physical barriers between the chambers and the stirring was conducted with magnetic rods at 500 rpm. Powders were weighed so that the amount of GBC was 10 mg in every chamber. Three parallel samples from crystalline compounds and six parallel from co-amorphous formulations were studied. The chambers were filled with HBSS-solution T=37 °C, pH 7.4 at 1 min intervals. Samples of 300 µl were taken at the following time points 15, 30, 45, 60, 75, 90, 120, 150, 180, 210, 240, 270, 300, 330 and 360 min which were replaced by the corresponding amount of HBSS-solution. Samples were filtered through 0.45 µm Jet Biofil® syringe filters (Guangzhou JET Bio-Filtration Co. Ltd, Guangzhou, China). For the crystalline GBC and physical mixtures, 150 µl of samples were pipetted into HPLC-tubes and diluted with 350 µl of acetonitrile (ACN). For amorphous GBC and the co-amorphous mixtures, 75 µl of samples were pipetted into HPLC-tubes and diluted first with 75 µl of ACN/H_2O (70:30) solution and subsequently with 350 µl of ACN. All samples were analyzed with an HPLC-UV-method. Degrees of supersaturation (DS) were calculated by dividing the concentrations of amorphous material obtained from the dissolution study with the experimentally determined equilibrium solubilities.

215 **2.7 Cell culturing**

MDCKII-MDR1 (the Netherlands Cancer Institute (Amsterdam, Netherlands)) cells were cultured in Dulbecco's modified Eagle medium (DMEM) supplemented with 10 % (V/V) fetal bovine serum (FBS) and 1 % penicillin-streptomycin (10 000 U/ml) according to the protocol reported by Hakkarainen et al., 2010. The cells were grown at 37 °C in 5 % of CO_2. The cells were subcultured twice a week when
220 the cells reached approximately 90 % confluency and used between passages 25-55.

2.8 Permeability studies

Permeability studies were conducted with MDCKII-MDR1 cells in similar side-by-side diffusion chambers and with similar settings as applied in the dissolution studies. The cells were calculated and
225 seeded in growth medium on Costar® filters (Corning Incorporated, New York, USA) at a cell density of 1.8×10^6 cells per filter (400 000 cells/cm^2). After seeding, the cells were grown on the filters for 3 days with the growth medium on both apical and basolateral side being changed daily. Prior to the permeability studies, the cell layer integrity was determined by measuring the TransEpithelial Electrical Resistance (TEER) values from each well with EVOM™ meter (World Precision Instruments Inc.,
230 Sarasota, Florida, USA). Then, Costar® filters with MDCKII-MDR1 cells were cut with a scalpel and placed between the chambers with the stirring in every chamber being performed with magnetic rods at 500 rpm. Samples were weighed and added to each chamber so that the amount of GBC was 10 mg in every chamber. Five parallel samples from every formulation were studied. The donor chambers were filled with 3 ml of pre-warmed HBSS, pH 7.4 containing 3 µl of D-[1-^{3}H(N)] labelled mannitol,
235 973.1 GBq/mmol (NEN Life Science Products, Boston, USA). Mannitol was used as a paracellular marker to monitor the integrity of the cell layer during the permeability studies. Simultaneously with the donor chambers, the acceptor chambers were filled with 3 ml of pre-warmed HBSS pH 7.4. Samples of 1 ml were taken from the acceptor chambers at the following time points 15, 30, 45, 60, 75, 90, 120, 150,

180, 210, 240, 270, 300, 330 and 360 min which were replaced by the corresponding amount of HBSS-solution.

For the quantification of mannitol permeated to the acceptor cells, 100 µl of the samples were pipetted into the radiometric microplates and diluted with 400 µl of Ultima Gold®. The amount of ^{3}H-labelled mannitol on the diffusion chambers was determined with a liquid scintillation and luminescence counter 1450 Microbeta Trilux® from PerkinElmer (Waltham, Massachusetts, USA). The rest of the samples (900 µl) were filtered through 0.45 µm Jet Biofil® syringe filters and 150 µl of filtered samples were pipetted into HPLC-tubes and diluted with 350 µl of acetonitrile (ACN). The samples were analyzed with the HPLC-UV-method as described below.

A preliminary permeability study with similar settings using crystalline GBC revealed that the integrity of the cell layer was retained for six hours when ^{3}H-labelled mannitol was used as a paracellular marker (data not shown). The permeability coefficients (P_{app}) were calculated as follows (Equation 3):

$$P_{app} = \frac{J}{C_d \times A} \quad \text{(Equation 3)},$$

in which J is the drug flux (mmol/cm^{2}s), C_d is the concentration in the donor chamber (mmol/cm^3) and A is the area of the cell layer (cm^2).

2.9 HPLC analysis

An HPLC system consisting of Gilson Pump 321, Autoinjector 234, Detector 151 and System Interface Module 506 C (Gilson, Villiers-le-Bel, France) was used and all samples were analyzed with the same method. A Gemini-NX 5 µm C18 110A (250 mm x 4.60 mm, Phenomenex Inc., Torrance, USA) was used as a column with a SecurityGuard precolumn (Phenomenex Inc., Torrance, USA) and Gilson Unipoint 3.0 software (Gilson, Middleton, USA) was used for data analysis. The mobile phase consisted of acetonitrile (ACN):H_2O: trifluoroacetic acid (TFA) (70:30:0.1, V/V/V), the isocratic flow was set to 1.2

ml/min and wavelength of 225 nm was used for GBC detection. For the calibration curve, a standard solution of 100 µg/ml was prepared in ACN/H_2O (70/30) from which dilutions of 0.1; 0.5; 5; 10; 25 and 50 µg/ml were prepared in ACN/H_2O.

265 **2.10 Data analysis**

Unpaired t-test with a confidence interval of 95 % and linear regression were used to compare the dissolution and permeability behavior. The AUCs were calculated from the concentration-time profile using linear trapezoidal integration. If $p<0.05$, the data were considered as statistically different. Prism GraphPad version 5.03 was used for data analysis (GraphPad Software Inc., La Jolla, California, USA).

270

3 Results and Discussion

3.1 Characterization of the co-amorphous mixtures

3.1.1 X-ray powder diffraction

The XRPD diffractograms (Fig. 2) indicated that both GBC-QRT CM and the QRT CM had been successfully transformed to amorphous forms as both formulations had a single halo in the XRPD diffractogram (Löbmann et al., 2013a). Instead, the reference diffractograms of crystalline GBC and QRT represented several peaks in their diffractograms (Fig. 2). The other formulations have been previously confirmed as being amorphous when cryomilled under similar conditions (Laitinen et al., 2014; Ruponen et al., 2018).

3.1.2 Differential scanning calorimetry

The T_g of the cryomilled GBC has been determined previously to be 71.9 °C (Laitinen et al., 2014), which was in accordance with the values for amorphous GBC prepared also by different methods (Mah et al., 2014; Patterson et al., 2005). The QRT CM was found to have a T_g value of 79.51 °C which is in accordance with the T_g value of amorphous QRT (83.79 °C) prepared by a solvent evaporation method (Table 1) (Dengale et al., 2015). In addition, a small recrystallization exotherm was seen at 110.5±0.3 °C (Fig. S1 in the Supplementary material). GBC-QRT CM was found to have a single glass transition temperature of T_g= 85.97 °C and a small recrystallization exotherm at 111.8±0.3 °C (Fig. S1 in the Supplementary material). A single T_g of GBC-QRT CM indicated that the mixture was homogeneously mixed and the components were fully miscible with each other (Chiou and Riegelman, 1971). By applying the Gordon-Taylor equation, the estimated T_g of GBC-QRT mixture was calculated to be 76.46 °C which is considerably lower than the experimentally detected value of T_g (Table 1). The positive deviation between the experimentally detected and calculated T_g suggests that intermolecular interactions between GBC and QRT molecules may have been formed (Ueda H et al., 2014). In addition,

the higher T_g value of GBC-QRT than the T_g of GBC may indicate better stability of the co-amorphous mixture as compared to pure amorphous GBC (Shamblin and Zografi, 1998; Yu, 2001).

3.1.3 Fourier-transform infrared spectroscopy

FTIR measurements were conducted to determine the possible molecular interactions between GBC and QRT. The other cryomilled formulations have been characterized previously (Laitinen et al., 2014; Ruponen et al., 2018). According to its FTIR-spectrum, GBC-SER CM was observed to form only weak interactions between GBC and SER (Laitinen et al., 2014). Instead, the spectrum of GBC-ARG CM revealed strong molecular interactions and a possible salt formation between the GBC and ARG molecules (Ruponen et al., 2018). Crystalline GBC showed characteristic carbonyl stretching at 1713 cm^{-1} and 1615 cm^{-1} (Fig. 3). The peaks present at 3310 cm^{-1} and 3364 cm^{-1} resulted from N–H stretching of the amide groups of GBC as reported previously (Laitinen et al., 2014; Wojnarowska et al., 2010). Crystalline QRT had a broad peak at 3281 cm^{-1} resulting from the O–H stretching of phenolic hydroxyl (OH) groups of QRT. Peaks at 1665 cm^{-1} and 1605 cm^{-1} were detected due to the stretching of carbonyl (C=O) group. Similar observations have been made previously (Dengale et al., 2015). The peak at 1509 cm^{-1} may be attributed to the aromatic group of QRT (Dengale et al., 2015).

QRT CM showed a broad, but significantly lower peak at 3350 cm^{-1}, when compared to crystalline QRT at 3281 cm^{-1}; this can be attributed to the general broadening of the peaks of amorphous material (Fig. 3). Peak shifts from the C=O stretching at 1665 cm^{-1} to 1649 cm^{-1} and at 1605 cm^{-1} to 1595 cm^{-1} were observed. Crystalline QRT's peak at 1509 cm^{-1} was slightly shifted to 1503 cm^{-1} with QRT CM. Similar minor alterations in the wavenumbers have been observed previously with amorphous QRT as a consequence of loss of the crystalline structure (Dengale et al., 2015).

The FTIR spectrum of GBC-QRT CM exhibited the changes associated with the characteristic peaks compared to the spectra of the crystalline compounds (Fig. 3). The C=O stretching peaks were observed to be broadened at 1713 cm^{-1} for amorphous GBC and at 1649 cm^{-1} for amorphous QRT. In addition, these peaks were further shifted to 1680 cm^{-1} and 1650 cm^{-1}, respectively, in GBC-QRT CM. The broad

peak at 3281 cm^{-1} in amorphous QRT was lowered, combined with the peak of amide N-H of amorphous GBC and shifted to higher wavenumbers (3368 cm^{-1}) indicating that hydrogen bonds may have been formed between QRT's hydroxyl groups and GBC's carbonyl groups (Fig. 3). This accounts for the deviation between the experimentally determined value of T_g and that of the $T_{g,mix}$ calculated with the Gordon-Taylor equation and are evidence that molecular interactions may have been formed between GBC and QRT (Ueda et al., 2014). Changes occurred also in the fingerprint region of the co-amorphous mixture. While both crystalline and amorphous GBC and QRT had sharp peaks between 1503 to 1531 cm^{-1}, no sharp peaks were observed with GBC-QRT CM.

3.2 Stability studies

The physical stabilities of GBC-QRT CM and QRT CM were tested during storage at the conditions of 4 °C/ 0 % RH, at 40 °C/ 0 % RH and room temperature (approximately 22 °C)/ 60 % RH.

QRT CM remained amorphous for at least 4 months at 4 °C/ 0 % RH as a similar amorphous halo was observed as had been present on day 0 (not shown). This was confirmed with FTIR measurements at 4 months (Fig. S2 in the Supplementary material). At 13 months, the halo of QRT CM at 4 °C/ 0 % RH showed peaks at similar angles as crystalline QRT indicating that the mixture had recrystallized (Fig. 4). At elevated temperature (40 °C/ 0 % RH), signs of recrystallization were observed in XRPD at 4 months (Fig. 4). The slightly shifted and enlarged peak resulting from the stretching of hydroxyl groups (OH) and slightly enlarged peaks in the fingerprint region were detected in FTIR measurements, confirming the XRPD results (Fig. S2 in the Supplementary material). At elevated humidity (room temperature/60 % RH), QRT CM showed the first signs of recrystallization according to XRPD after 10 days of storage (Fig. 4).

GBC-QRT CM was found to be amorphous after 13 months of storage at 4 °C/ 0 % RH and at elevated temperature according to XRPD (Fig. 4). No peak shifts or changes in the FTIR-spectra were observed confirming the XRPD results (Fig. S3 in the Supplementary material).

At elevated humidity (room temperature/60 % RH), the first signs of recrystallization were observed after 30 days of storage with GBC-QRT CM (Fig. 4). A minor peak was observed at 26.5° indicative of an alteration in the solid-state structure. A broadening and enlargement of the peak may have resulted from the crystallization of QRT since the peak was located at an angle specific to QRT (Fig. 2). Thus, compared to the other mixtures examined in this study, GBC-QRT seems to be more sensitive to moisture, as GBC-ARG has been demonstrated to be stable for at least 18 months and GBC-ARG-SLS mixtures for at least 11 months under all storage conditions (Ruponen et al., 2018). However, GBC-QRT was more stable than amorphous GBC and GBC-SER, since these materials showed signs of recrystallization at 5 months and six months, respectively, at 4 °C/0% RH and at 40 °C/0% RH.

3.3 The equilibrium solubility of GBC in HBSS

The equilibrium solubility values of crystalline GBC and GBC in physical mixtures are presented in Table 2. There were no statistical differences between GBC-SER and GBC-QRT and the pure crystalline GBC (Table 2). Nonetheless, GBC-ARG and GBC-ARG-SLS did display significant differences in terms of GBC solubility as compared to crystalline GBC. The increase in the solubility of GBC-ARG may be explained by the presence of ARG which has been reported to form salts with different molecules (Lenz et al., 2015) and act as a solubility enhancer of poorly water soluble drugs through intermolecular interactions (Hirano et al., 2010; Miranda et al., 2018). In their study, Miranda et al. (2018) noted that there was a linear ARG concentration dependent increase in the solubility of a poorly water soluble drug furosemide. Similar observations have been reported by Hirano et al. (2010) i.e. the solubility of alkyl gallates increased sharply in the presence of ARG due to the aromatic structures of alkyl gallates.

Aromatic structures which may interact with the guanidinium group of ARG can be found also in GBC (Ruponen et al., 2018).

Interestingly, there was no significant increase in the solubility GBC-ARG-SLS in comparison with GBC-ARG, although SLS as a surfactant is known to act as a solubility enhancer (Table 2) (Indulkar et al., 2017). The lack of improvement of solubility may result from the small concentration of SLS, as the improvement generally occurs after the critical micelle concentration (CMC) has been exceeded (Indulkar et al., 2017; Stephenson et al., 2006).

3.4 Dissolution properties

The dissolution profiles of crystalline GBC and physical mixtures (PM) of GBC-SER and GBC-QRT were found to be similar (Fig. 5a). With these formulations, the equilibrium solubilities of GBC (6.86 µg/ml) and the physical mixtures (5.53 and 7.85 µg/ml) were reached after 90 minutes (Fig. 5a and Table 2). In the case of GBC-ARG PM and GBC-ARG-SLS PM, the concentrations of dissolved GBC were approximately doubled at 6 hours in comparison with the other formulations; this is probably attributable to the higher equilibrium solubility of these mixtures (Table 2). They reached their equilibrium solubility within 75 minutes. The calculated AUCs followed a similar order, as the AUC values of crystalline GBC, GBC-SER PM and GBC-ARG PM were almost identical whereas GBC-ARG PM and GBC-ARG-SLS PM differed significantly, i.e. with 2.8 and 3.6-fold higher values compared to crystalline GBC, from other formulations (Fig. 7a). The total cumulative amounts of dissolved GBC with each formulation followed a similar order as the observed concentrations (Fig. S4 in Supplementary material). These results are in accordance with previous publications (Heikkinen et al., 2015; Ruponen et al., 2018).

In the dissolution studies, the co-amorphous mixtures exhibited significantly higher dissolved GBC concentrations as compared to their corresponding physical mixtures (Fig. 5b). Cryomilled GBC displayed a supersaturated state at 15 min (Fig. 5b). When compared to crystalline GBC, a 17-fold supersaturation was observed at C_{max} with GBC CM (Fig. 6). A typical spring effect for pure amorphous

compounds (Brouwers et al., 2009) was seen with GBC CM as the concentration declined quickly after T_{max} approaching the equilibrium solubility of crystalline GBC. The calculated AUC value of GBC CM was 8-fold higher compared to crystalline GBC (Fig. 7).

GBC-SER CM showed a 10-fold supersaturation at C_{max} compared to the corresponding physical mixture (Fig. 6). A spring effect was seen also with GBC-SER CM, although to a lesser extent than with GBC CM as the increase was smaller and the concentration remained virtually unchanged after 150 min (Fig. 5b). The small improvement in the dissolution of GBC-SER CM may result from the weak interactions formed between GBC and SER molecules (Laitinen et al., 2014). Similar observations have been made in previous studies (Heikkinen et al., 2015; Ruponen et al., 2018).

The dissolution profile of GBC-QRT CM differed significantly from GBC-QRT PM and cryomilled GBC and GBC-SER (Fig. 5b). The AUC value of GBC-QRT CM was 20-fold higher than the corresponding physical mixture (Fig. 7). The concentration increased rapidly for 210 minutes resulting in a 24-fold supersaturation as compared to the physical mixture at C_{max} (Fig. 6). Although a decrease in the concentration was observed after 210 min, a noticeable supersaturation was maintained for 6 hours. The increased concentrations may be attributed to the amorphization of the material as amorphous compounds often display a clearly increased dissolution profile in comparison to physical mixtures (Jensen et al., 2015; Laitinen et al., 2013). The significantly increased concentration of GBC-QRT CM when compared to both GBC CM and GBC-SER CM may result from the possible hydrogen bonding between GBC and QRT as detected by FTIR. As previously stated, interactions between the components of the co-amorphous mixture may increase not only the physical stability but also maintain the supersaturated state during dissolution (Ojarinta et al., 2017; Ruponen et al., 2018).

The co-amorphous mixtures of GBC-ARG and GBC-ARG-SLS exhibited significantly higher concentrations of dissolved GBC than the other formulations in the dissolution studies (Fig. 5b). The calculated AUC values were 19-fold (GBC-ARG) and 21-fold (GBC-ARG-SLS) higher and significantly different from the values of the corresponding physical mixtures (Fig. 7). This finding is in accordance

with previous reports (Ruponen et al., 2018). GBC-ARG CM showed over 18-fold supersaturation at 120 min when compared to the corresponding physical mixture while GBC-ARG-SLS CM resulted in a nearly 31-fold supersaturation at C_{max} at 150 min (Fig. 6). The results for GBC-ARG CM and GBC-ARG-SLS CM may be accounted for by the amorphization of the material, the strong interactions observed between GBC and ARG (Lenz et al., 2015; Ruponen et al., 2018) and the solubilizing effect of ARG via aromatic interactions (Hirano et al., 2010; Ruponen et al., 2018).

Although no difference was seen in the equilibrium solubility between GBC-ARG and GBC-ARG-SLS, GBC-ARG-SLS CM showed slightly higher concentrations in the dissolution study (Fig. 5b). Furthermore, the AUC value for GBC-ARG-SLS was 1.5-fold higher and statistically significantly different from the AUC value of GBC-ARG CM (Fig. 7). At odds with this observation, in the previous study, GBC-ARG CM showed a higher amount of dissolved GBC than GBC-ARG-SLS CM mixture (Ruponen et al., 2018). It was suggested that this difference was may be due to sulphonyl groups of GBC and the SLS molecules which had interfered with the sulfonyl-mediated interactions between GBC and ARG. The contradictory dissolution results of the two studies might be due to the differences (pH, ionic content etc.) between the dissolution media, i.e. phosphate buffer used by Ruponen et al. and HBSS.

The total cumulative amount of dissolved GBC with cryomilled formulations followed a similar order as the physical mixtures, with the exception of GBC-QRT CM, which showed a slightly increased amount of dissolved GBC as compared to GBC CM and GBC-SER CM (Fig. S4 in the Supplementary material).

3.5 Permeability properties of the co-amorphous mixtures

The permeability studies of co-amorphous mixtures were evaluated in the side-by-side diffusion chambers separated by the MDCKII-MDR1 cell layer, enabling simultaneous dissolution of the powder sample in the donor chamber and drug permeation across the cell layer. There was a non-steady state

situation in the permeability assay as the dry powders were constantly dissolving in the donor chambers after which they permeated through the MDCKII-MDR1 cell layer. In addition, continuous dissolution of GBC from the powder replaced the permeated amount of GBC in the donor chamber. Preliminary studies investigating the cytotoxicity of the prepared co-amorphous mixtures indicated that the integrities of the cell layers were not altered significantly during the six hours' test (Fig. S5 in the Supplementary material).

With the physical mixtures, the amounts of GBC which succeeded in permeating through the cell layer were below the limit of quantification (0.1 µg/ml) with the exception of the physical mixture of GBC-ARG-SLS. GBC-ARG-SLS PM showed a linear increase in the total amount of GBC permeating through the cell layer (Fig. 8a). GBC-ARG-SLS PM showed the highest dissolution of the physical mixtures, resulting in the highest concentration gradient of the physical mixtures promoting the flux (Sinko, 2011). The same observation was made in the studies with the PAMPA membrane (Ruponen et al., 2018). In addition, SLS can affect the tight junctions of cells and thus increase the test compound's paracellular permeability (Yu et al., 2013). The effect of SLS on cell integrity was seen as an increase in the P_{app} values for mannitol (Table S1 in the Supplementary material).

In the case of the co-amorphous mixtures, GBC CM, GBC-SER CM and GBC-QRT CM permeated through the cell layer to a similar extent as GBC-ARG-SLS PM (Fig. 8). This may be due to the similarity of their dissolution properties (Fig. 5-7). Although QRT is known to be a P-glycoprotein (Pgp) inhibitor and thus capable of preventing possible drug efflux (Choi et al., 2011), no difference was observed in the permeating amount of GBC or in the AUC values between GBC CM and GBC-QRT CM (Fig. 8a). In the dissolution study, GBC-QRT CM maintained a higher supersaturated state and a higher concentration than GBC CM, resulting in a higher concentration gradient promoting the flux (Fig. 5b). GBC is mainly absorbed via the transcellular route by passive diffusion and thus inhibiting Pgp and the efflux may not alter in the amount of permeating GBC (Zerrouk et al., 2006). Thus, it may be possible, that the effect of inhibitors would only be clearly seen with those poorly permeable class IV drugs for which Pgp efflux

has a significant impact (Ghadi and Dand, 2017a). The similarity in the permeability profile may also result from GBC's Pgp-inhibiting property. Although GBC is known to be a substrate of Pgp also some inhibitory potential has been observed (Ghadi and Dand, 2017b). With GBC CM, Pgp may be inhibited by GBC molecules and GBC-QRT CM QRT and GBC might be competing inhibitors.

GBC-ARG CM and GBC-ARG-SLS CM exhibited the highest cumulative amounts of permeated GBC (Fig. 8a). This is in accordance with the results from the dissolution studies and previous studies in which the permeability of these mixtures through a PAMPA membrane has been investigated (Ruponen et al., 2018). Interestingly, there was no statistical difference in the amount of permeating GBC between GBC-ARG CM and GBC-ARG-SLS CM (Fig. 8a). With the physical mixtures, a difference was seen, this being probably due to the presence of SLS; however with the cryomilled mixtures, the improved dissolution might override the effect of SLS, as there was a significantly greater concentration gradient than could be achieved with the physical mixtures of both GBC-ARG and GBC-ARG-SLS (Fig. 5). Combining GBC with ARG seems to be beneficial with respect to permeability as the AUC values of both GBC-ARG and GBC-ARG-SLS differed significantly from the other cryomilled formulations (Fig. 8b). The AUC values of GBC-ARG CM and GBC-ARG-SLS CM were over 3-fold and 4-fold higher than the corresponding value of GBC CM. This may be mostly explained by the better dissolution profile of these mixtures (Fig. 5b) in comparison with the other cryomilled mixtures. Another explanation for the improved permeation may be the permeability enhancing property of ARG, although the mechanism behind this phenomenon is still rather unclear (Motlekar et al., 2006). Motlekar et al. (2006) reported that ARG enhanced the permeability of heparin through a Caco-2 monolayer. Furthermore, it has been reported that ARG can act as a permeability enhancer of insulin, stimulating its oral absorption (Kamei et al., 2017). This finding was supported by the permeability coefficients of GBC in which ARG exerted as notable an effect i.e. GBC-ARG CM and GBC-ARG-SLS CM showed higher P_{app} values than the other cryomilled formulations (Table S1 in the Supplementary material).

The calculated AUCs from the concentration-time profiles followed a similar order as the total cumulative amounts of permeated GBC. Linear regression analysis revealed that there was a good correlation between the AUC values of permeability and dissolution (r^2=0.9775) (Fig. 9). This suggests that increasing the dissolution might be the main mechanism behind the enhancement of permeability observed with the selected excipients.

4 Conclusions

In this study, the effect of co-amorphization was investigated on the dissolution and permeability properties of a poorly water soluble drug, (a biopharmaceutical classification system (BCS) class II compound), glibenclamide (GBC) with different amino acids (AA), a Pgp-inhibitor (QRT) and a surfactant (SLS). The characterization of the cryomilled GBC-QRT revealed a single T_g value indicating that an amorphous homogeneous single phase system had been formed with intermolecular interactions. Consequently, the mixture was found to be stable for at least 13 months when stored at 4 °C/0 % RH and at 40 °C/0%.

In the simultaneous dissolution and permeability experiments using MDCKII cell layer overexpressing Pgp as a permeation barrier, a linear correlation was detected between the AUC values of permeability and dissolution of the formulations. This suggested that increasing the dissolution by formation of the co-amorphous mixture might be the primary effect enhancing the permeability with the selected excipients. Particularly, the Pgp inhibitor QRT was not found to show any specific permeation-enhancing effect for GBC. The co-amorphous combinations showing the most significant enhancement of drug dissolution were GBC-ARG CM and GBC-ARG-SLS CM, with 19- and 21-fold increases in the AUC values for dissolution when compared to the corresponding physical mixtures. Furthermore, GBC-ARG-SLS CM showed a 9-fold higher value of AUC for permeability than the corresponding physical mixture.

This permeability model with side-by-side diffusion chambers with MDCKII cells proved to be a feasible and cost-effective method for evaluating the permeability properties of amorphous compounds as the cell layers remained sufficiently intact despite the stress caused by the dissolution of the dry powders, the permeation of the compounds and the rather long duration of the permeability test. Furthermore, the results suggest that with appropriate cell models and study set-ups, it would also be possible to study the impact of active drug transport in detail in the future, which is impossible with artificial membranes, such as PAMPA.

Acknowledgements

The authors would like to thank Mrs. Lea Pirskanen for her cell culturing expertise and professional technical assistance. This research did not receive any specific grant from funding agencies in the public, commercial, or not-for-profit sectors.

5 References

Allesø M, Chieng N, Rehder S, Rantanen J, Rades T, Aaltonen J, 2009: Enhanced dissolution rate and synchronized release of drugs in binary systems through formulation: Amorphous naproxen–cimetidine mixtures prepared by mechanical activation. J. Control. Release 136, 45-53,

Beyer A, Grohganz H, Löbmann K, Rades T, Leopold C, 2017: Improvement of the physicochemical properties of Co-amorphous naproxen-indomethacin by naproxen-sodium. Int. J. Pharm. 526, 88-94, http://dx.doi.org/10.1016/j.ijpharm.2017.04.011

Brouwers J, Brewster M, Augustijns P, 2009: Supersaturating Drug Delivery Systems: The Answer to Solubility-Limited Oral Bioavailability?. J. Pharm. Sci. 98, 2549-2572, http://dx.doi.org/10.1002/jps.21650

Byrn S, McKenzie A, Hassan M, Al-Badr A, 1986: Conformation of glyburide in the solid state and in solution. J. Pharm. Sci. 75, 596-600, http://dx.doi.org/10.1002/jps.2600750615

Chiou W, Riegelman S, 1971: Pharmaceutical applications of solid dispersion systems. J. Pharm. Sci. 60, 1281-1302, http://dx.doi.org/10.1002/jps.2600600902

Choi J, Piao Y, Kang K, 2011: Effects of quercetin on the bioavailability of doxorubicin in rats: role of CYP3A4 and P-gp inhibition by quercetin. Arch. Pharm. Res. 34, 607-613, http://dx.doi.org/10.1007/s12272-011-0411-x

Dengale S, Grohganz H, Rades T, Löbmann K, 2016: Recent advances in co-amorphous drug formulations. Adv. Drug. Deliv. Rev. 100, 116-125, http://dx.doi.org/10.1016/j.addr.2015.12.009

Dengale S, Hussen S, Krishna B, Musmade P, Shenoy G, Bhat K, 2015: Fabrication, solid state characterization and bioavailability assessment of stable binary amorphous phases of Ritonavir with Quercetin. Eur. J. Pharm. Biopharm. 89, 329-338, http://dx.doi.org/10.1016/j.ejpb.2014.12.025

Ghadi R, Dand N, 2017a: BCS class IV drugs: Highly notorious candidates for formulation development. J. Control. Rel. 248, 71-95. http://dx.doi.org/10.1016/j.jconrel.2017.01.014

Ghadi R, Dand N, 2017b: P-glycoprotein inhibition by glibenclamide and related compounds. Pflugers. Arch. 437, 652-660, http://dx.doi.org/10.1007/s004240050829

Hakkarainen JJ, Jalkanen AJ, Kääriäinen TM, Keski-Rahkonen P, Venäläinen T, Hokkanen J, Mönkkönen J, Suhonen M, Forsberg MM, 2010: Comparison of in vitro cell models in predicting in vivo brain entry of drugs. Int. J. Pharm. 402, 27-36, http://dx.doi.org/10.1016/j.ijpharm.2010.09.016

Hauss D, 2007: Oral lipid-based formulations. Adv. Drug. Deliv. Rev. 59, 667-676, http://dx.doi.org/10.1016/j.addr.2007.05.006

Heikkinen A, DeClerk L, Löbmann K, Grohganz H, Rades T, Laitinen R, 2015: Dissolution properties of co-amorphous drug-amino acid formulations in buffer and biorelevant media. Pharmazie 70, 452–457, http://dx.doi.org/10.1691/ph.2015.4210

Hirano A, Kameda T, Arakawa T, Shiraki K, 2010: Arginine-Assisted Solubilization System for Drug Substances: Solubility Experiment and Simulation. J. Phys. Chem. B 114, 13455–13462, http://dx.doi.org/10.1021/jp101909a

Indulkar A, Mo H, Gao Y, Raina S, Zhang G, Taylor L, 2017: Impact of Micellar Surfactant on Supersaturation and Insight into Solubilization Mechanisms in Supersaturated Solutions of Atazanavir. Pharm. Res. 34, 1276–1295, http://dx.doi.org/10.1007/s11095-017-2144-0

Jensen K, Larsen F, Cornett C, Löbmann K, Grohganz H, Rades T, 2015: Formation Mechanism of Coamorphous Drug–Amino Acid Mixtures. Mol. Pharm. 12, 2484–2492, http://dx.doi.org/10.1021/acs.molpharmaceut.5b00295

Kamei N, Khafagy E, Hirose J, Takeda-Morishita M, 2017: Potential of single cationic amino acid molecule “Arginine” for stimulating oral absorption of insulin. Int. J. Pharm. 521, 179-183, http://dx.doi.org/10.1016/j.ijpharm.2017.01.066

Kasten G, Nouri K, Grohganz H, Rades T, Löbmann K, 2017: Performance comparison between crystalline and co-amorphous salts of indomethacin-lysine. Int. J. Pharm. 533, 138-144, http://dx.doi.org/10.1016/j.ijpharm.2017.09.063

Kataoka M, Tsuneishi S, Maeda Y, Masaoka Y, Sakuma S, Yamashita S, 2014: A new in vitro system for evaluation of passive intestinal drug absorption: establishment of a double artificial membrane permeation assay. Eur. J. Pharm. Biopharm. 88, 840-846, http://dx.doi.org/10.1016/j.ejpb.2014.09.009

Laitinen R, Löbmann K, Grohganz H, Priemel P, Strachan C, 2017: Supersaturating drug delivery systems: The Potential of co-amorphous drug formulations. Int. J. Pharm. 532, 1-12, http://dx.doi.org/10.1016/j.ijpharm.2017.08.123

Laitinen R, Löbmann K, Grohganz, H, Strachan C, Rades T, 2014: Amino Acids as Co-amorphous Excipients for Simvastatin and Glibenclamide: Physical Properties and Stability. Mol. Pharm. 11, 2381−2389, http://dx.doi.org/10.1021/mp500107s

Laitinen R, Löbmann K, Strachan C, Grohganz H, Rades T, 2013: Emerging trends in the stabilization of amorphous drugs. Int. J. Pharm. 453, 65-79, http://dx.doi.org/10.1016/j.ijpharm.2012.04.066

Lenz E, Jensen K, Blaabjerg L et al., 2015: Solid-state properties and dissolution behaviour of tablets containing co-amorphous indomethacin–arginine. Eur. J. Pharm. Biopharm. 96, 45-52, http://dx.doi.org/10.1016/j.ejpb.2015.07.011

Lipinski C, Lombardo F, Dominy B, Feeney P, 2001: Experimental and computational approaches to estimate solubility and permeability in drug discovery and development settings. Adv. Drug. Deliv. Rev., 46, 3-26. http://dx.doi.org/10.1016/S0169-409X(00)00129-0

Löbmann K, Grohganz H, Laitinen R, Strachan C, Rades T, 2013a: Amino acids as co-amorphous stabilizers for poorly water soluble drugs − Part 1: preparation, stability and dissolution enhancement. Eur. J. Pharm. Biopharm. 85, 873−881, http://dx.doi.org/10.1016/j.ejpb.2013.03.014

Löbmann K, Laitinen R, Grohganz H, Gordon K, Strachan C, Rades T, 2011: Coamorphous Drug Systems: Enhanced Physical Stability and Dissolution Rate of Indomethacin and Naproxen. Mol. Pharm. 8, 1919–1928, http://dx.doi.org/10.1021/mp2002973

Löbmann K, Laitinen R, Strachan C, Rades T, Grohganz H, 2013b: Amino acids as co-amorphous stabilizers for poorly water-soluble drugs – Part 2: Molecular interactions. Eur. J. Pharm. Biopharm. 85, 882-888, http://dx.doi.org/10.1016/j.ejpb.2013.03.026

Löbmann K, Strachan C, Grohganz H, Rades T, Korhonen O, Laitinen R, 2012: Co-amorphous simvastatin and glipizide combinations show improved physical stability without evidence of intermolecular interactions. Eur. J. Pharm. Biopharm. 81, 159-169, http://dx.doi.org/10.1016/j.ejpb.2012.02.004

Mah P, Laaksonen T, Rades T, Aaltonen J, Peltonen L, Strachan C, 2014: Unravelling the Relationship between Degree of Disorder and the Dissolution Behavior of Milled Glibenclamide. Mol. Pharm. 11, 234-242, http://dx.doi.org/10.1021/mp4004145

Mesallati H, Conroy D, Hudson S, Tajber L, 2017: Preparation and characterization of amorphous ciprofloxacin-amino acid salts. Eur. J. Pharm. Biopharm. 121, 73-89, http://dx.doi.org/10.1016/j.ejpb.2017.09.009

Miranda J, Garnero C, Zoppi A, Sterren V, Ayala A, Longhi M, 2018: Characterization of systems with amino-acids and oligosaccharides as modifiers of biopharmaceutical properties of furosemide. J. Pharmaceut. Biomed. Anal. 149, 143–150, http://dx.doi.org/10.1016/j.jpba.2017.10.038

Motlekar N, Srivenugopal K, Wachtel M, Youan B, 2006: Modulation of gastrointestinal permeability of low-molecular-weight heparin by L-arginine: in-vivo and in-vitro evaluation. J. Pharm Pharmacol. 58, 591-598, http://dx.doi.org/10.1211/jpp.58.5.0003

Ojarinta R, Heikkinen A, Sievänen E, Laitinen R, 2017: Dissolution behavior of co-amorphous amino acid-indomethacin mixtures: The ability of amino acids to stabilize the supersaturated state of indomethacin. Eur. J. Pharm. Biopharm. 112, 85-95, http://dx.doi.org/10.1016/j.ejpb.2016.11.023

Patterson J, James M, Forster A, Lancaster R, Butler J, Rades T, 2005: The Influence of Thermal and Mechanical Preparative Techniques on the Amorphous State of Four Poorly Soluble Compounds. J. Pharm. Sci. 94, 1998-2012, http://dx.doi.org/10.1002/jps.20424

Ruponen M, Visti M, Ojarinta R, Laitinen R, 2018: Permeability of glibenclamide through a PAMPA membrane: the effect of co-amorphization. Eur. J. Pharm. Biopharm. 129, 247-256, http://dx.doi.org/10.1016/j.ejpb.2018.06.007

Shamblin S, Zografi G, 1998: Enthalphy Relaxation in binary Amorphous Mixtures Containing Sucrose. Pharm. Res. 15, 1828-1834, http://dx.doi.org/10.1023/A:1011997721086

Sinko P: Diffusion. In a book: Martin's Physical Pharmacy and Pharmaceutical Sciences. 6th Edition, pp. 223-257. Editor: Troy D, Lippincott Williams & Wilkins, a Wolters Kluwer business, Baltimore 2011

Sironi D, Christensen M, Rosenberg J, Bauer-Brandl A, Brandl M, 2017: Evaluation of a dynamic dissolution/permeation model: Mutual influence of dissolution and barrier-flux under non-steady state conditions. Int. J. Pharm. 522, 50-57, http://dx.doi.org/10.1016/j.ijpharm.2017.03.002

Srirangam P, Vidya Sagar J, 2010: Modulation of the P-Glycoproein-Mediated Intestinal Secretion of Glibenclamide: In Vitro and In Vivo Assessments. J. Young. Pharm. 2, 379-383 http://dx.doi.org/10.4103/0975-1483.71632

Stephenson B, Rangel-Yagui C, Pessoa Junior A, Tavares L, Beers K, Blankschtein D, 2006: Experimental and Theoretical Investigation of the Micellar-Assisted Solubilization of Ibuprofen in Aqueous Media. Langmuir 22, 1514–1525, http://dx.doi.org/10.1021/la052530k

Ueda H, Aikawa S, Kashima Y et al., 2014: Anti-plasticizing Effect of Amorphous Indomethacin Induced by Specific Intermolecular Interactions with PVA Copolymer. J. Pharm. Sci. 103, 2829-2838, http://dx.doi.org/10.1002/jps.24023

Vasisht K, Chadha K, Karan M, Bhalla Y, Jena AK, Chadha R, 2016: Enhancing biopharmaceutical parameters of bioflavonoid quercetin by cocrystallization. CrystEngComm 18, 1403-1415, http://dx.doi.org/10.1039/C5CE01899D

Williams H, Trevaskis N, Charman S et al., 2013: Strategies to Address Low Drug Solubility in Discovery and Development. Pharmacol. Rev. 65, 315-499, http://dx.doi.org/10.1124/pr.112.005660

Wojnarowska Z, Grzybowska K, Adrjanowicz K et al., 2010: Study of the Amorphous Glibenclamide Drug: Analysis of the Molecular Dynamics of Quenched and Cryomilled Material. Mol. Pharm. 7, 1692–1707, http://dx.doi.org/10.1021/mp100077c

Yu L, 2001: Amorphous pharmaceutical solids: preparation, characterization and stabilization. Adv. Drug. Deliv. Rev. 48, 27-42, http://dx.doi.org/10.1016/S0169-409X(01)00098-9

Yu Q, Wang Z, Li P, Yang Q, 2013: The effect of various absorption enhancers on tight junction in the human intestinal Caco-2 cell line. Drug Dev. Ind. Pharm. 39, 587-592, http://dx.doi.org/10.3109/03639045.2012.692376

Zerrouk N, Corti G, Ancillotti S, Maestrelli F, Cirri M, Mura P, 2006: Influence of cyclodextrins and chitosan, separately or in combination, on glyburide solubility and permeability. Eur. J. Pharm. Biopharm. 63, 241-246, http://dx.doi.org/10.1016/j.ejpb.2005.08.010

Table 1. Glass transition temperatures (T_g) of amorphous GBC and QRT and cryomilled mixtures (°C)

Sample	T_g (Experimental)	T_g (Literature)	$T_{g,mix}$ (Calculated)
GBC CM	na[a]	71.9 ± 0.7[b]	na
QRT CM	79.51 ± 0.99	83.79 ± 1.79[c]	na
GBC-QRT 1:1 CM	85.97 ± 0.29	na	76.46
GBC-SLS 1:1 CM	na	54.4 ± 1.0; 68.9 ± 1.3[d]	na
GBC-SER 1:1 CM	na	70.1 ± 1.3[b]	na
GBC-ARG 1:1 CM	na	62.8 ± 1.78[d]	na
GBC-ARG-SLS CM	na	61.2 ± 0.1[d]	na

[a] na = Not analyzed (or not applicable)

[b] From Laitinen R et al., 2014

[c] Amorphous QRT by solvent evaporation method. From Dengale et al., 2015

[d] From Ruponen et al., 2018

Table 2. The equilibrium solubilities of GBC and the physical mixtures (n=3)

Sample	Solubility (µg/ml)
GBC	6.86 ± 0.89
GBC-ARG	22.68 ± 1.98[a]
GBC-SER	5.53 ± 1.78
GBC-QRT	7.85 ± 1.67
GBC-ARG-SLS	23.19 ± 7.80[a]

[a] Statistically significantly different ($p<0.05$) when compared to GBC

Figure legends

Figure 1. Chemical structures of the drugs and the excipients: a) Glibenclamide (GBC), b) L-arginine (ARG), c) L-serine (SER), d) Quercetin (QRT) and e) Sodium lauryl sulphate (SLS)

Figure 2. XRPD diffractograms for crystalline GBC and QRT and cryomilled QRT and GBC-QRT mixtures on day 0.

Figure 3. FTIR-spectra of crystalline GBC and QRT and GBC-QRT CM and QRT CM on day 0. * from Laitinen et al. 2014.

Figure 4. XRPD diffractograms of a) GBC-QRT CM 13 months at 4 °C/ RH 0 %, b) GBC-QRT CM after 13 months 40 °C/ RH 0 %, c) GBC-QRT CM on day 30 at room temp./ RH 60 %, d) QRT CM after 13 months at 4 °C/ RH 0 %, e) QRT CM on day 132 at 40 °C/ RH 0 %, f) QRT CM on day 10 at room temp./ RH 60 %

Figure 5. Dissolved GBC concentrations (mean µg/ml ± SD) in HBSS pH 7.4 as a function of time for a) Crystalline (CRYS) GBC and physical mixtures (PM) (n=3) and b) Cryomilled GBC and co-amorphous mixtures (n=6). Please note the scales of the vertical axes.

Figure 6. Degree of supersaturation (mean ± SD) as a function of time for cryomilled mixtures (n=6) in HBSS pH 7.4.

Figure 7. Area under curve (AUC, µg x min/ml ± SD) values calculated from the concentrations of GBC in HBSS pH 7.4 for a) dissolution of physical mixtures (n=3), b) dissolution of co-amorphous mixtures (n=6). * stands for statistically significant difference as compared to the corresponding physical mixture. Please note scale of the vertical axes.

Figure 8. a) The total cumulative amount of GBC permeating (m(GBC), mg ± SD, n=5, except with GBC-ARG-SLS PM n=3) through the MDCKII-MDR1 cell layer as a function of time (min) in HBSS at pH 7.4. b) Area under curve (AUC, µg x min/ml ± SD, n=5, with the exception of GBC-ARG-SLS PM n=3) values calculated from the concentrations of GBC in HBSS at pH 7.4 in the permeability study. * Stands for statistically significantly different value as compared to GBC CM.

Figure 9. Areas under curve (AUC) calculated in the permeability study (n=5) as a function of AUC values from the dissolution study (n=6, with the exception of GBC-ARG-SLS PM n=3). a) GBC-SER CM, b) GBC-ARG-SLS PM, c) GBC CM, d) GBC-QRT CM, e) GBC-ARG CM, f) GBC-ARG-SLS CM.

Figures

Fig 1

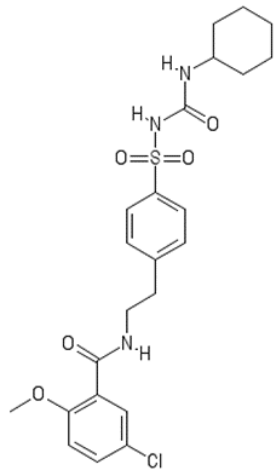

GBC

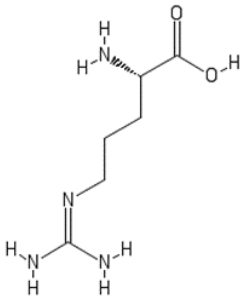

ARG

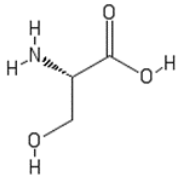

SER

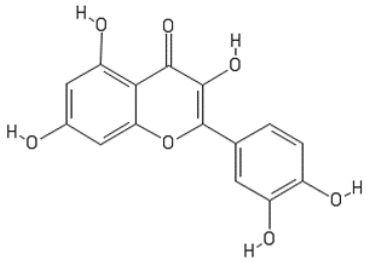

QRT

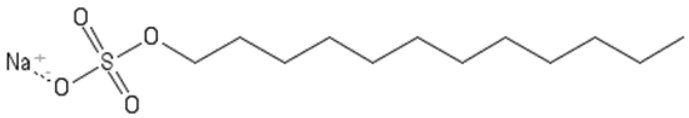

SLS

Fig 2

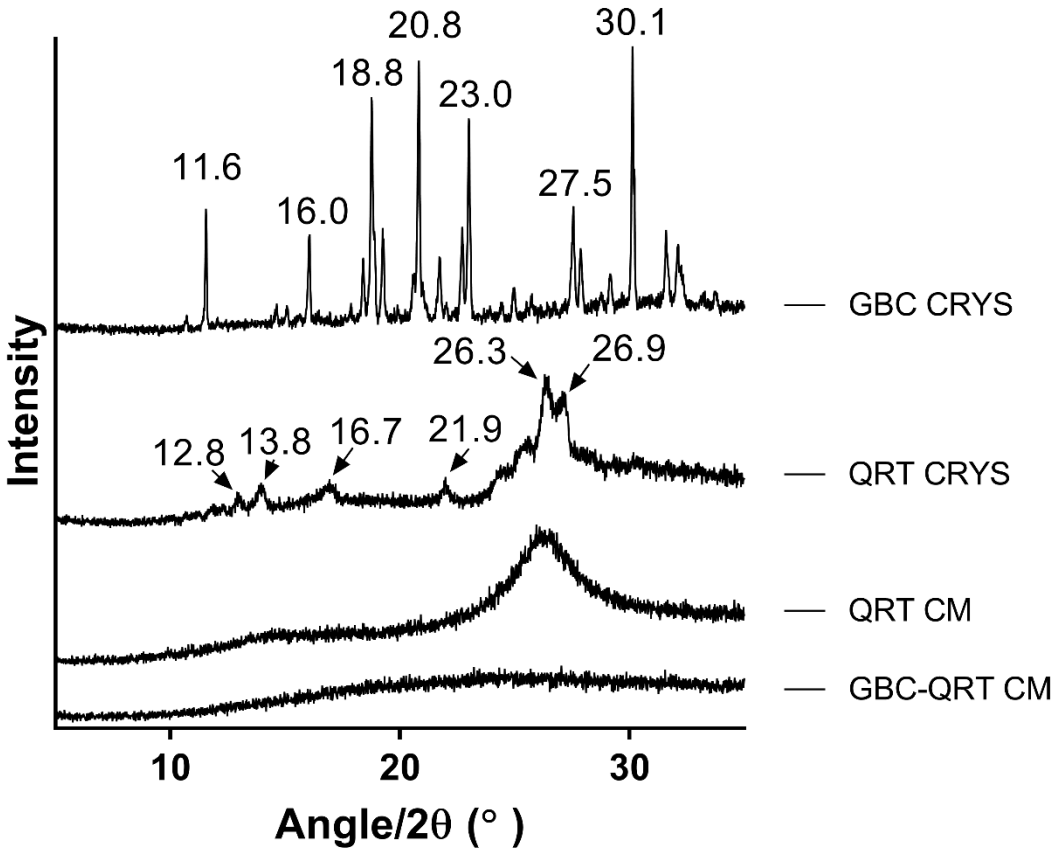
20.8
30.1
18.8
23.0
11.6
16.0
27.5
GBC CRYS
26.3
26.9
12.8
13.8
16.7
21.9
QRT CRYS
QRT CM
GBC-QRT CM
Intensity
10
20
30
Angle/2θ (°)

Fig 3

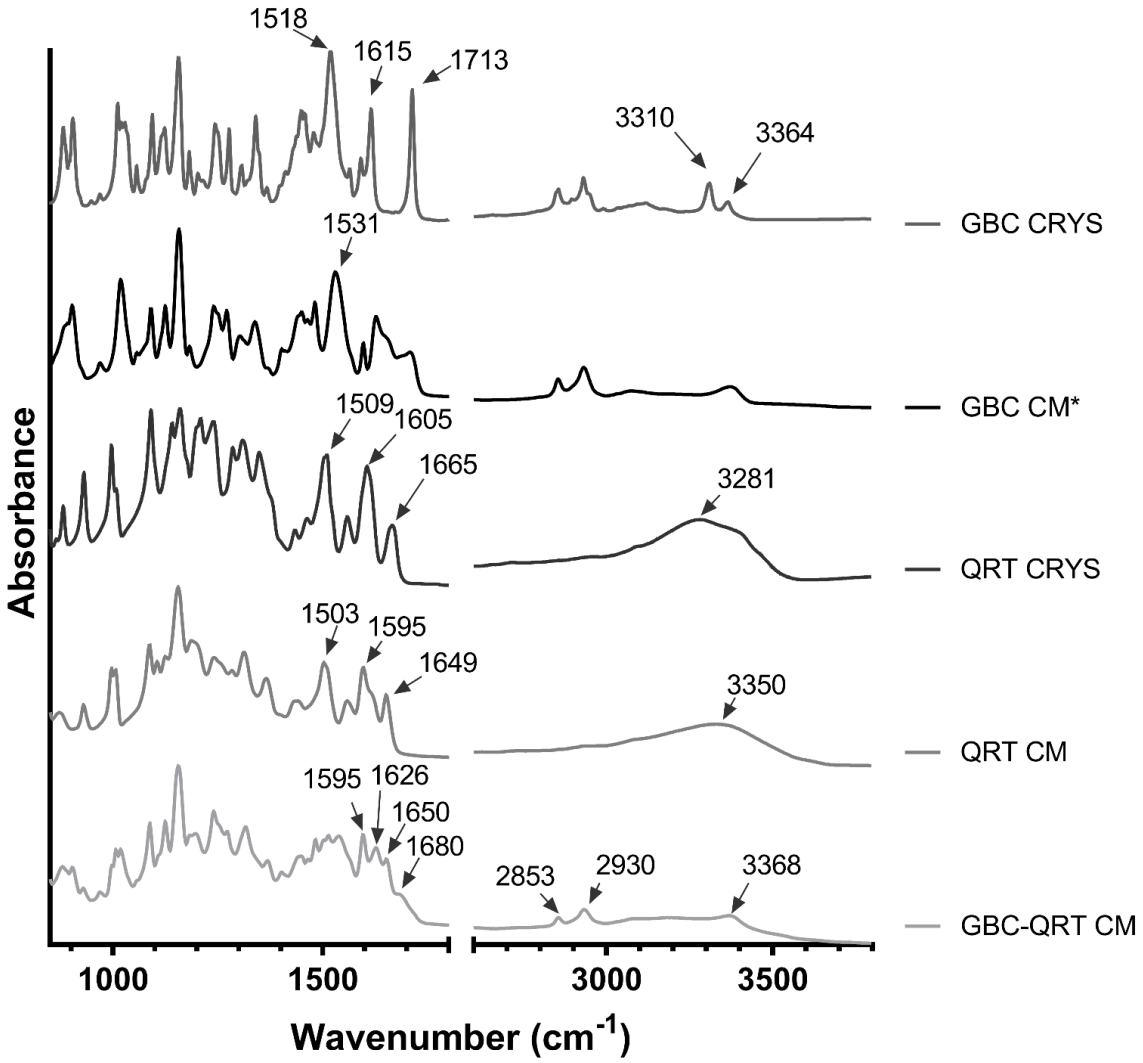
1518
1615
1713
3310
3364
GBC CRYS
1531
GBC CM*
1509
1605
1665
3281
QRT CRYS
1503
1595
1649
3350
QRT CM
1595
1626
1650
1680
2853
2930
3368
GBC-QRT CM
Absorbance
1000
1500
3000
3500
Wavenumber (cm-1)

Fig 4

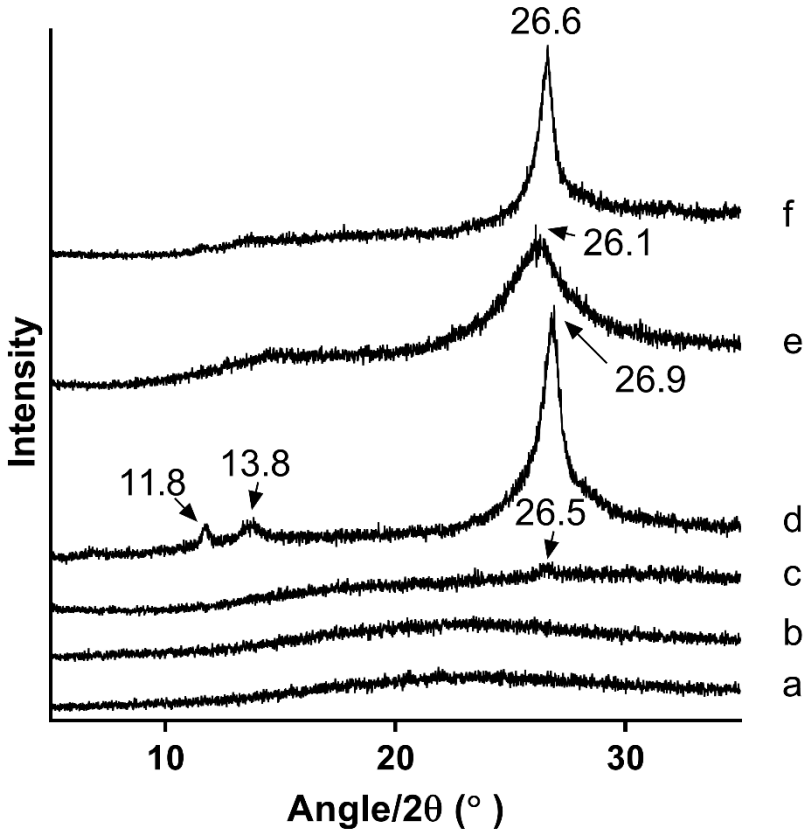

Fig. 5a

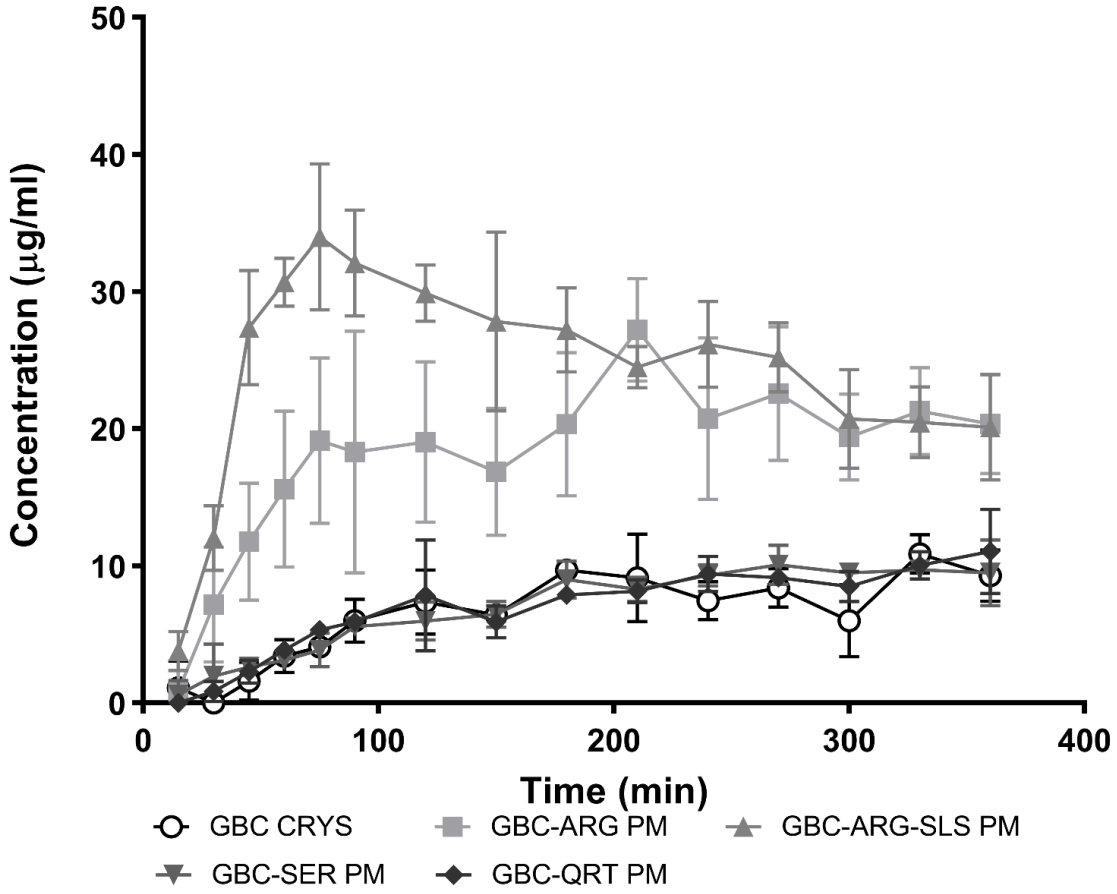
Concentration (µg/ml)
50
40
30
20
10
0
0
100
200
300
400
Time (min)
GBC CRYS
GBC-ARG PM
GBC-ARG-SLS PM
GBC-SER PM
GBC-QRT PM

Fig 5b

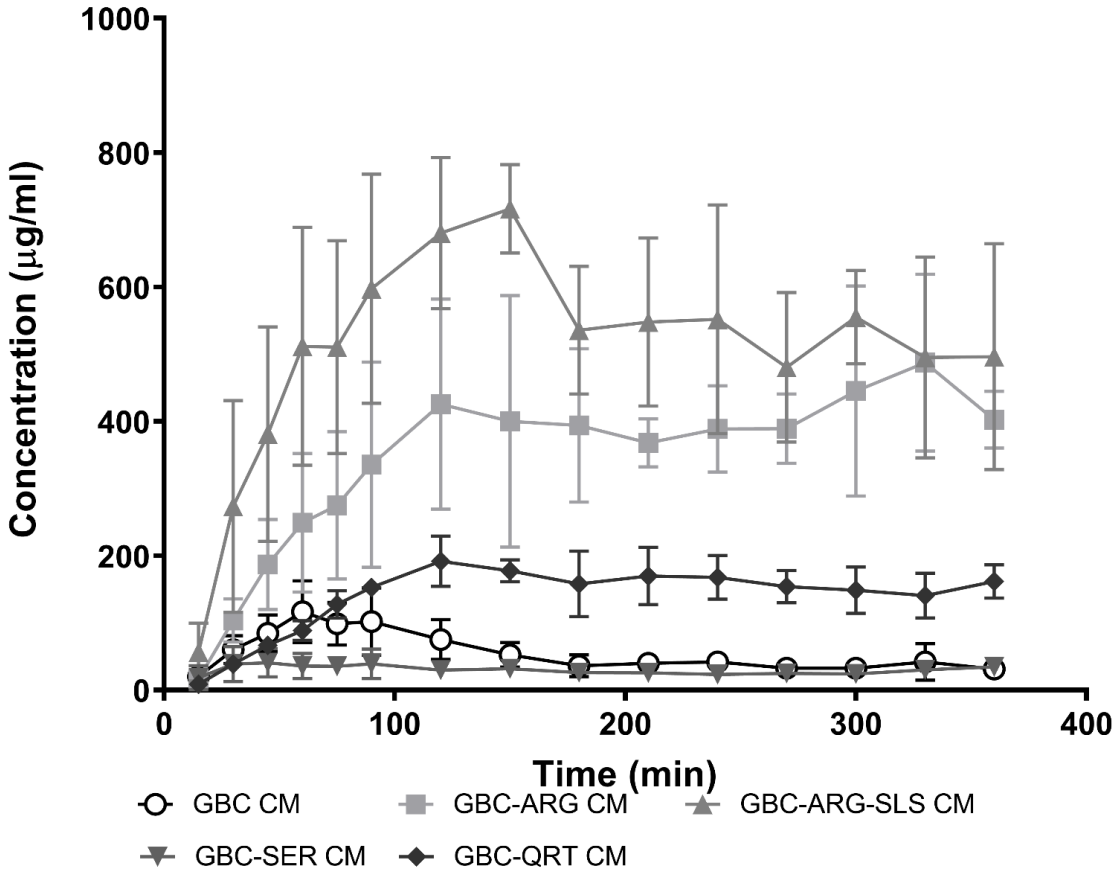
Concentration (µg/ml)
1000
800
600
400
200
0
0
100
200
300
400
Time (min)
GBC CM
GBC-ARG CM
GBC-ARG-SLS CM
GBC-SER CM
GBC-QRT CM

Fig 6

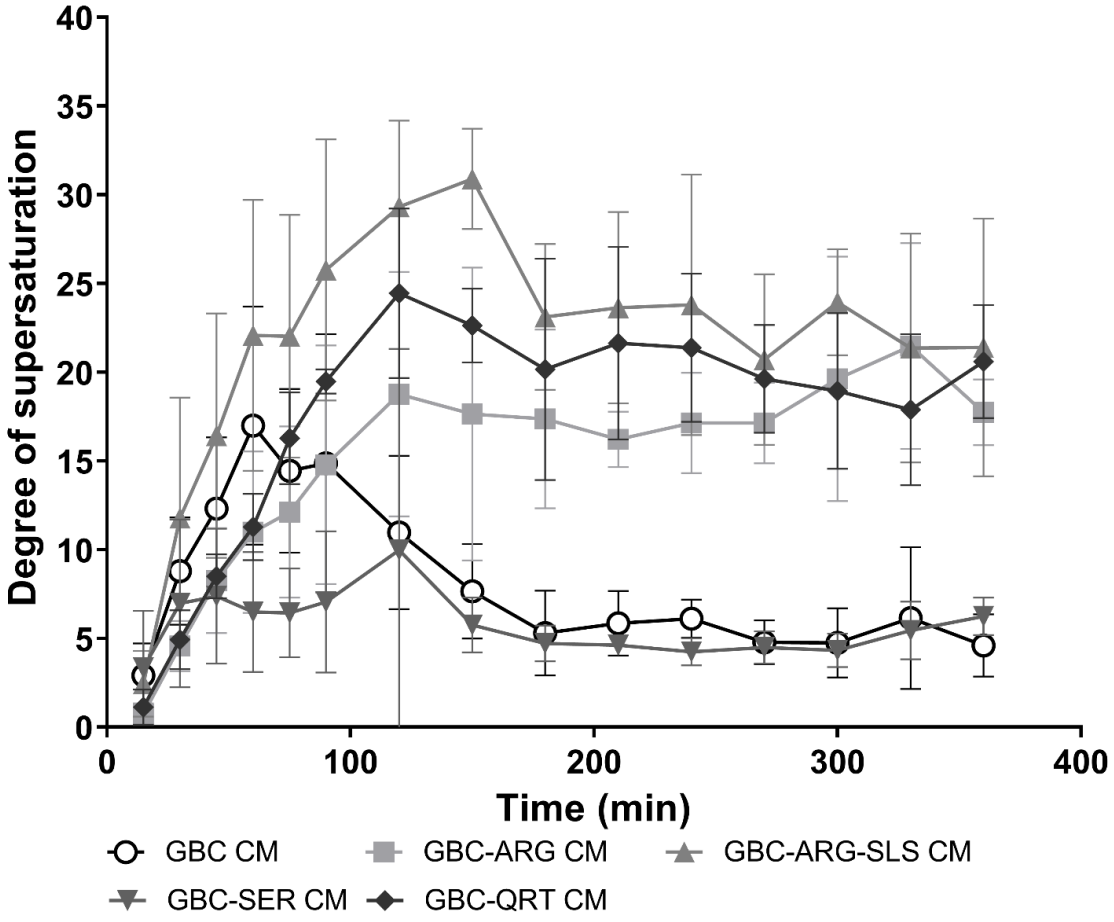
Degree of supersaturation
40
35
30
25
20
15
10
5
0
0
100
200
300
400
Time (min)
GBC CM
GBC-ARG CM
GBC-ARG-SLS CM
GBC-SER CM
GBC-QRT CM

Fig7a

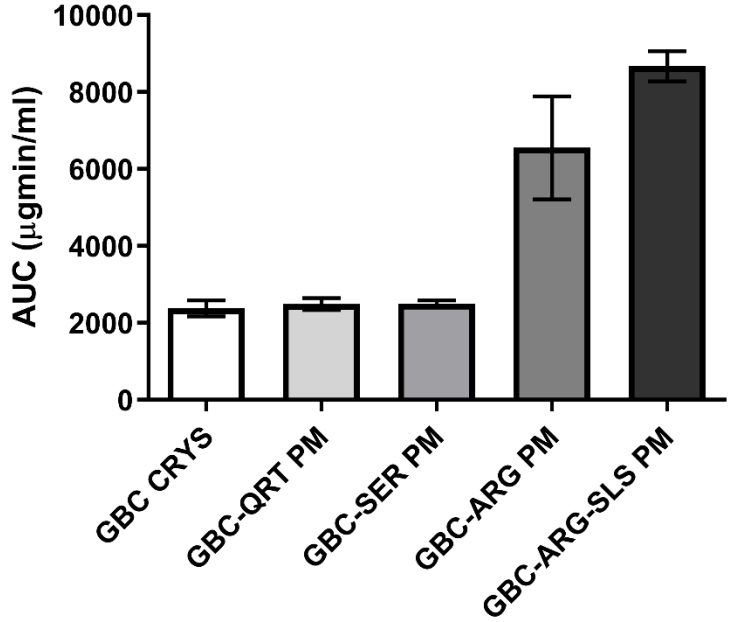
AUC (μgmin/ml)
10000
8000
6000
4000
2000
0
GBC CRYS
GBC-QRT PM
GBC-SER PM
GBC-ARG PM
GBC-ARG-SLS PM

Fig 7b

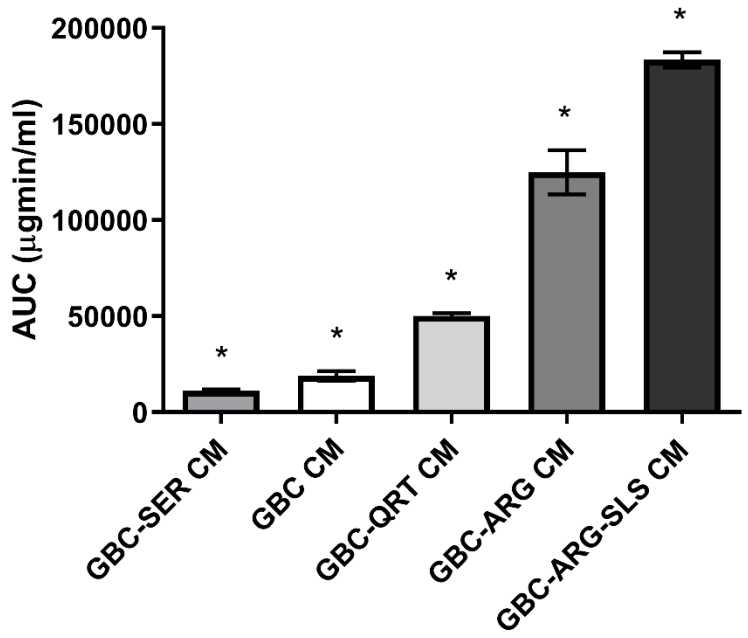
AUC (μgmin/ml)
200000
150000
100000
50000
0
*
*
*
*
*
GBC-SER CM
GBC CM
GBC-QRT CM
GBC-ARG CM
GBC-ARG-SLS CM

Fig 8a

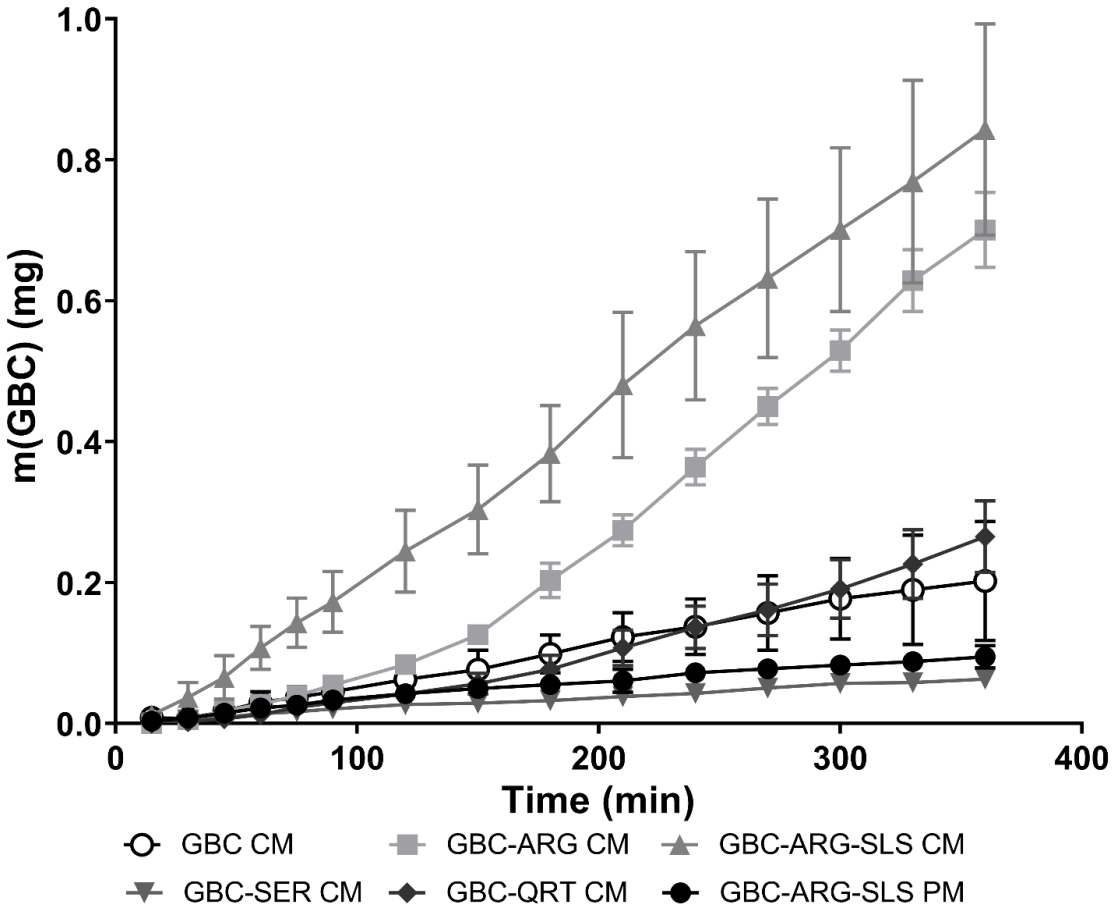
m(GBC) (mg)
1.0
0.8
0.6
0.4
0.2
0.0
0
100
200
300
400
Time (min)
GBC CM
GBC-ARG CM
GBC-ARG-SLS CM
GBC-SER CM
GBC-QRT CM
GBC-ARG-SLS PM

Fig 8b

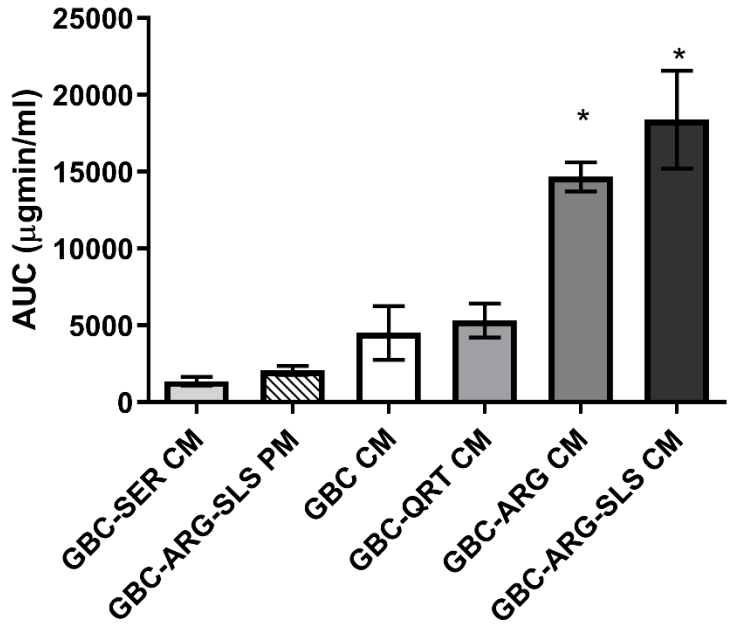
25000
20000
15000
10000
5000
0
AUC (μgmin/ml)
*
*
GBC-SER CM
GBC-ARG-SLS PM
GBC CM
GBC-QRT CM
GBC-ARG CM
GBC-ARG-SLS CM

Fig 9

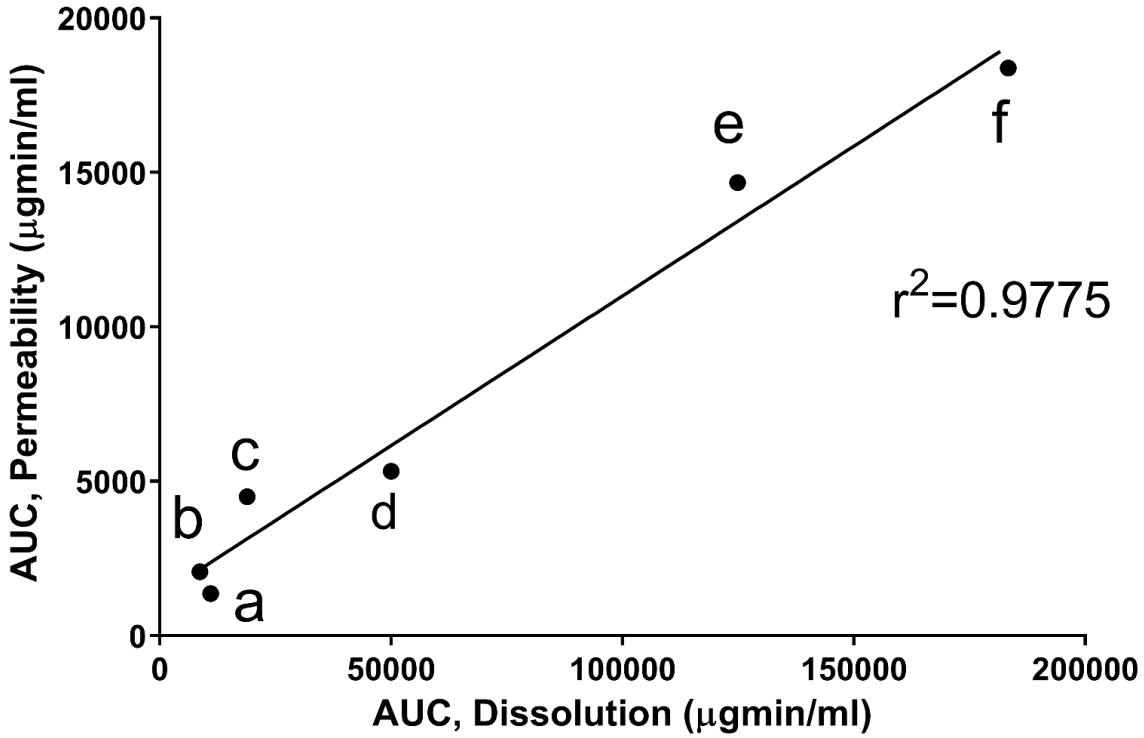
20000
15000
10000
5000
0
AUC, Permeability (μgmin/ml)
a
b
c
d
e
f
r2=0.9775
0
50000
100000
150000
200000
AUC, Dissolution (μgmin/ml)

Supplementary material for "The effect of co-amorphization of glibenclamide on its dissolution properties and permeability through an MDCKII-MDR1 cell layer" by Sormunen et al.

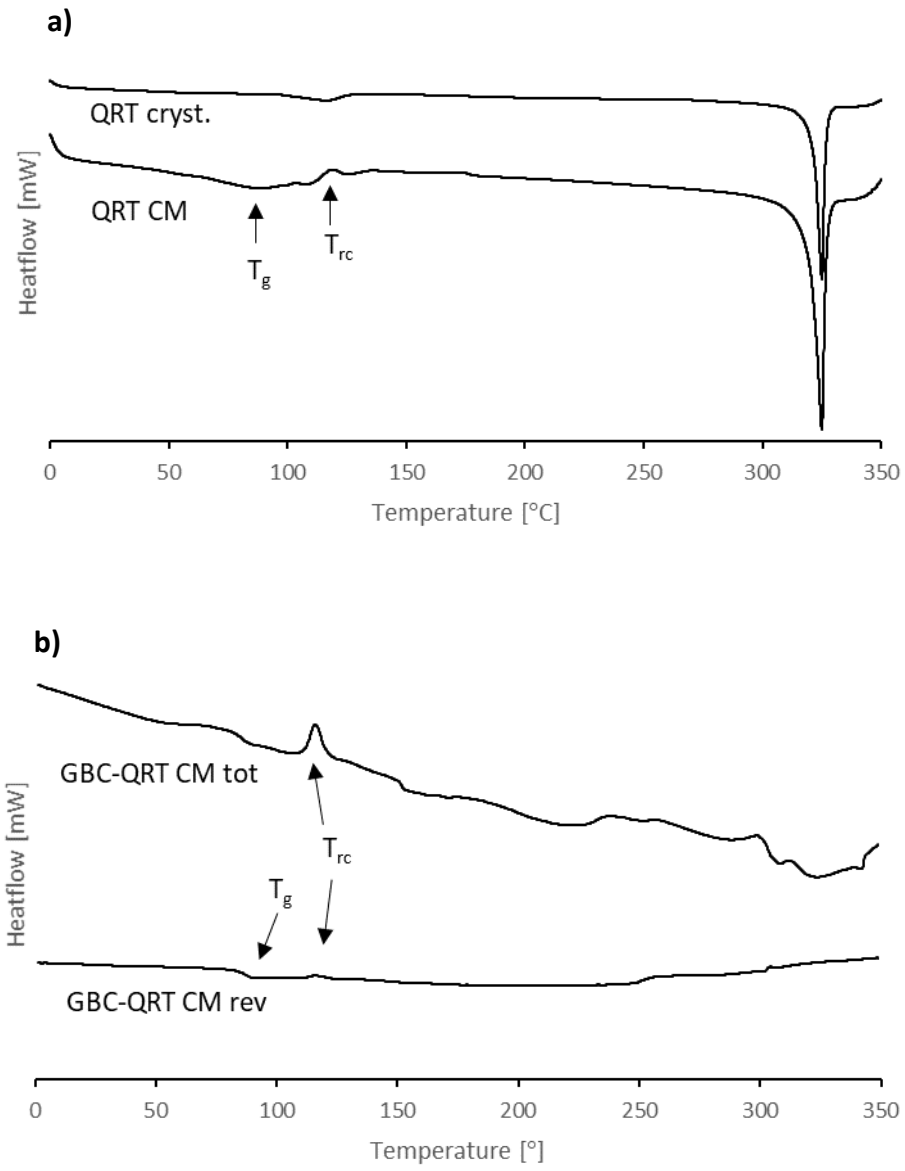

Figure S1. DSC-thermograms of a) crystalline QRT and QRT CM, b) GBC-QRT CM, showing the reversing and total heatflow curves.

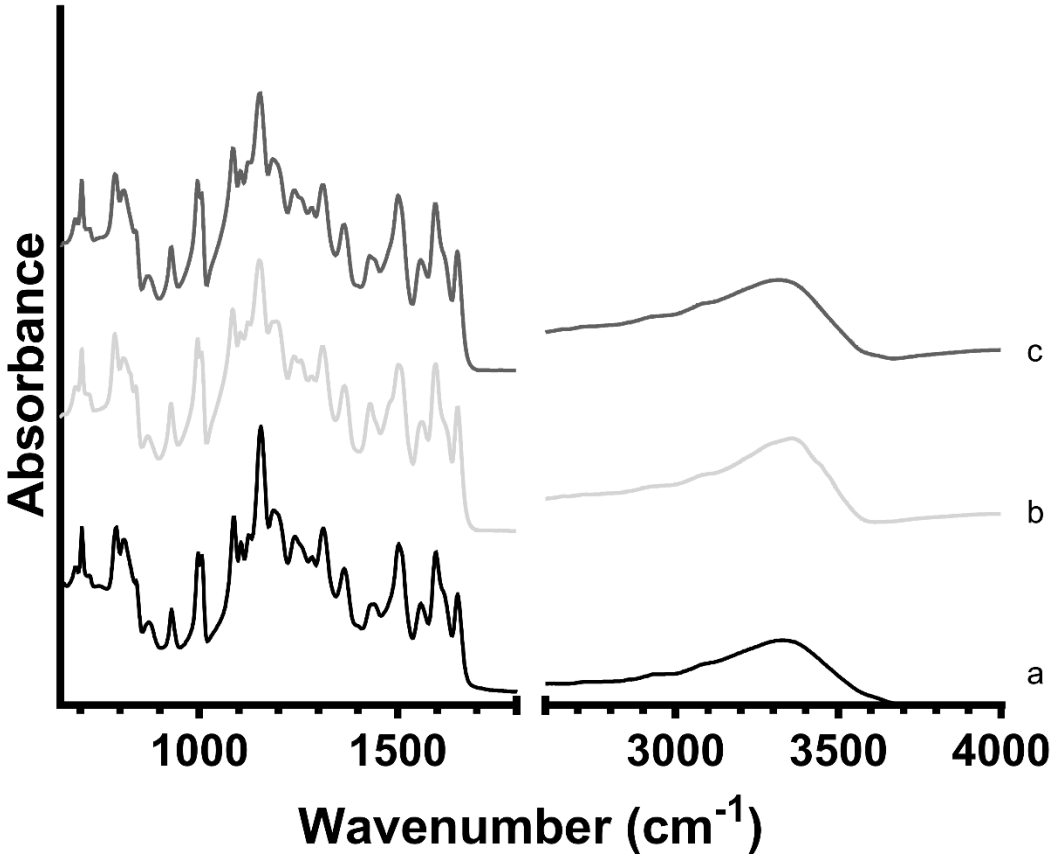

Figure S2. FTIR-spectra of a) QRT CM at day 0, b) QRT CM on day 132 at 40 °C/ 0 % RH, c) QRT CM on day 132 at 4 °C/ 0 % RH

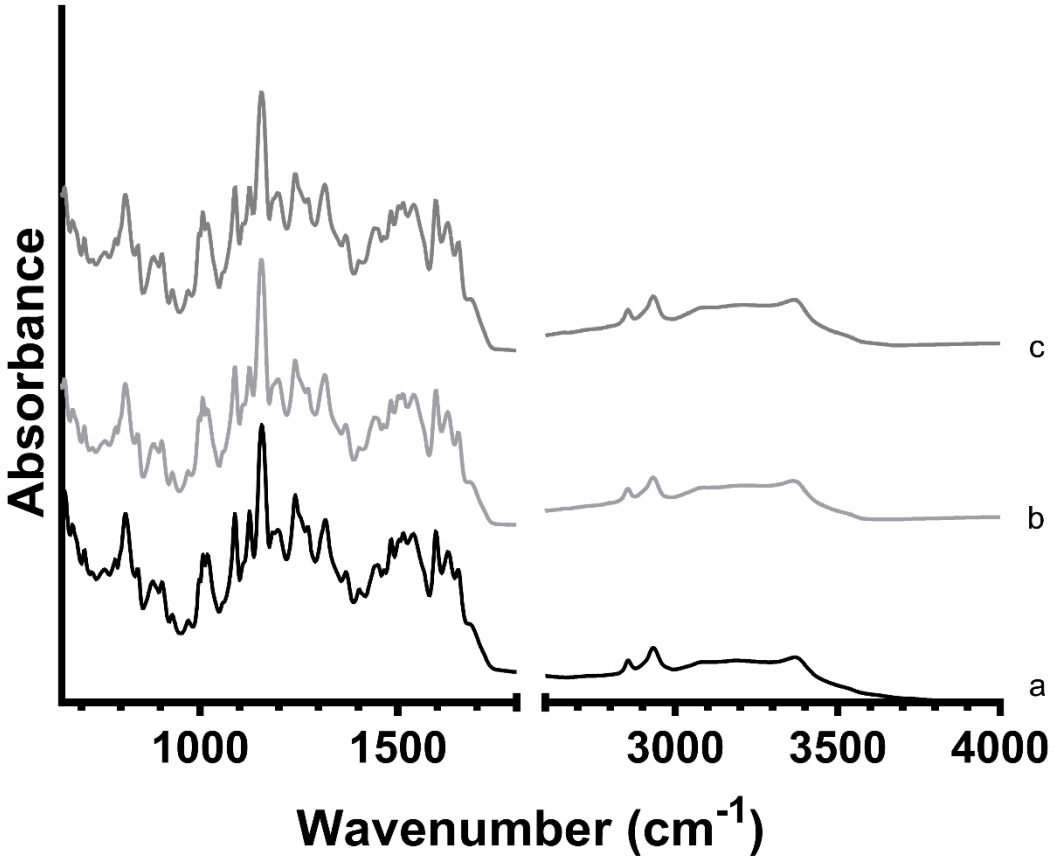

Figure S3. FTIR-spectra of a) GBC-QRT CM at day 0, b) GBC-QRT CM after 13 months at 40 °C/ 0 % RH, c) GBC-QRT CM after 13 months at 4 °C/ 0 % RH

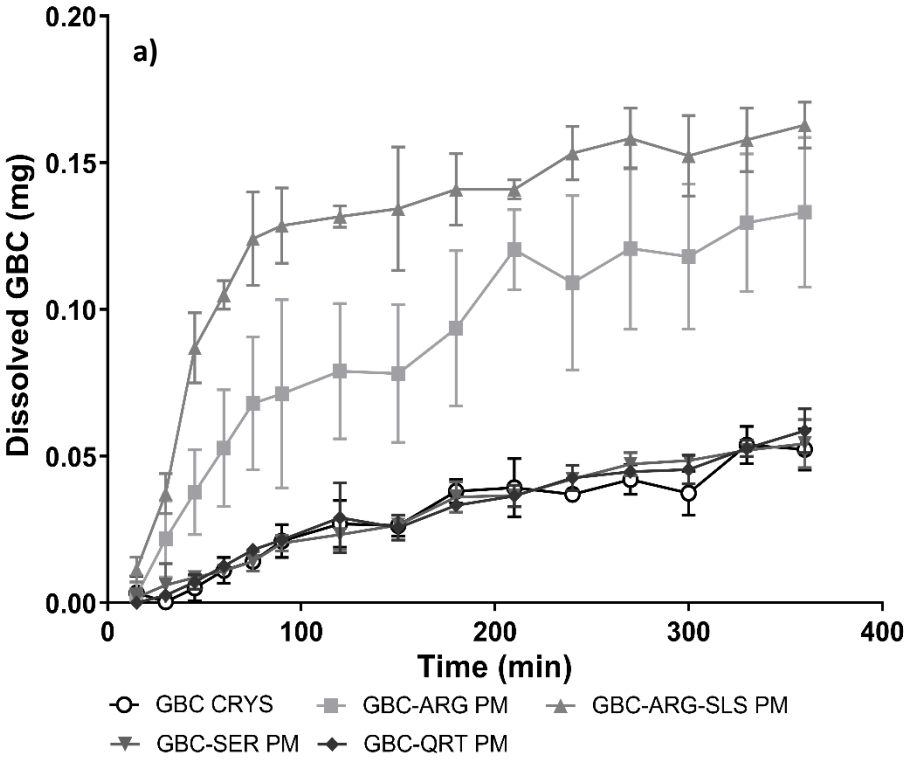
a)
Dissolved GBC (mg)
0.20
0.15
0.10
0.05
0.00
0
100
200
300
400
Time (min)
GBC CRYS
GBC-ARG PM
GBC-ARG-SLS PM
GBC-SER PM
GBC-QRT PM

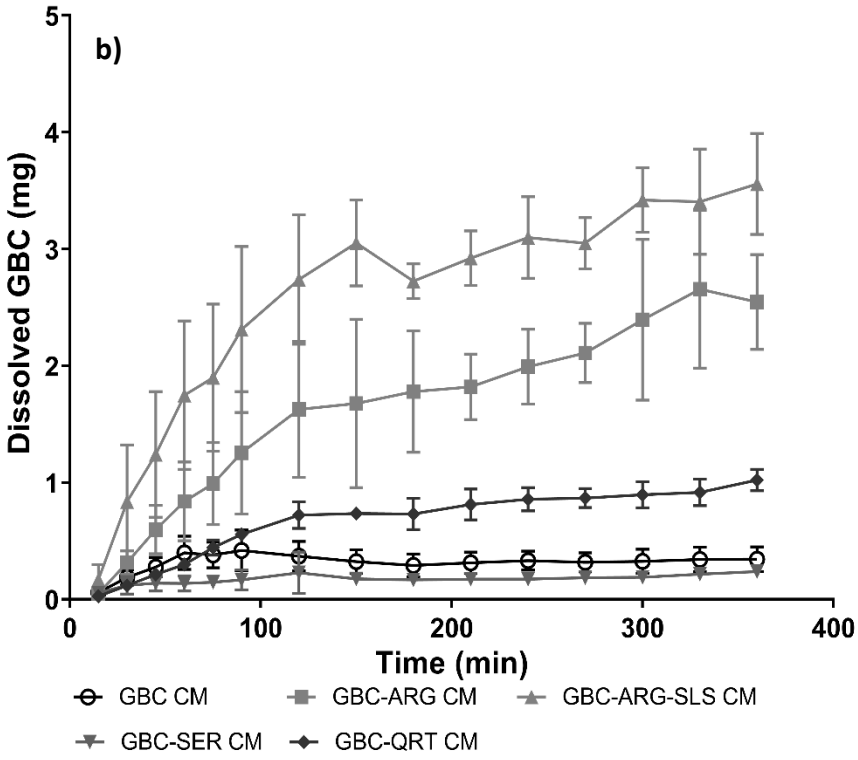
b)
Dissolved GBC (mg)
5
4
3
2
1
0
0
100
200
300
400
Time (min)
GBC CM
GBC-ARG CM
GBC-ARG-SLS CM
GBC-SER CM
GBC-QRT CM

Figure S4. Total cumulative amount of dissolved GBC (mean mg ± SD) in HBSS pH 7.4 as a function of time for a) Crystalline (CRYS) GBC and physical mixtures (PM) (n=3) and b) Cryomilled GBC and co-amorphous mixtures (n=6)

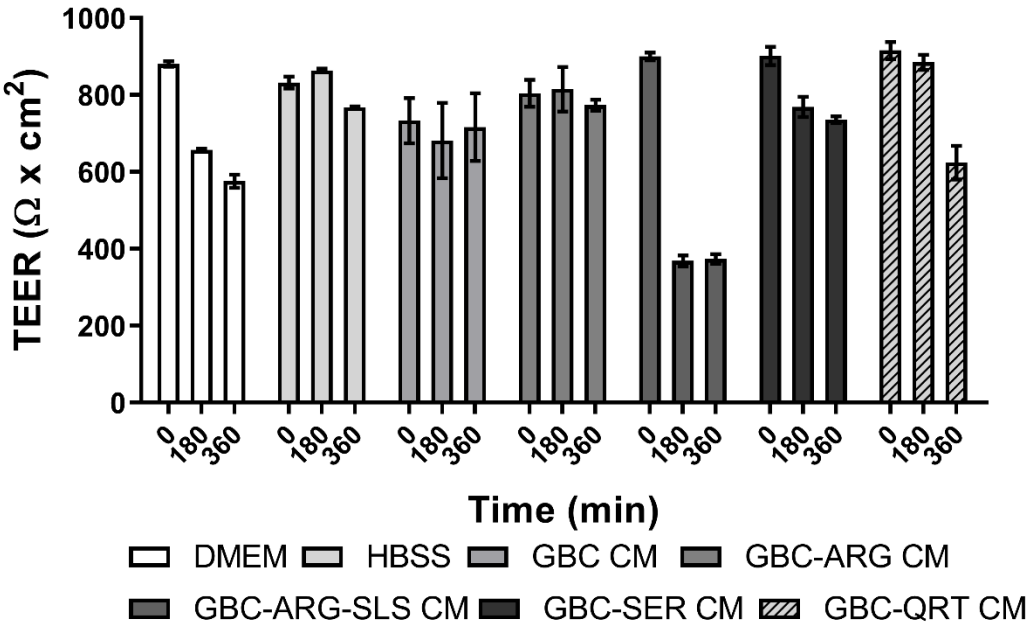

Figure S5. TEER-values (Ω x cm^2) at different time points during the toxicity study.

Table S1. Permeability coefficients (P_{app}) for GBC and Mannitol (cm/s)

Sample	P_{app} x 10^{-6} for GBC, n=5 with CM, n=3 with GBC-ARG-SLS PM	P_{app} x 10^{-6} for Mannitol, n=5 with CM, n=3 with PM
GBC CM	4.72 ± 3.21	20.44 ± 3.35
GBC-ARG CM	21.38 ± 1.79	39.78 ± 3.26
GBC-SER CM	1.29 ± 0.44	23.52 ± 1.22
GBC-QRT CM	7.73 ± 1.56	45.87 ± 27.83
GBC-ARG-SLS CM	19.93 ± 3.59	23.88 ± 5.33
GBC CRYS	na[a]	10.19 ± 6.34
GBC-ARG PM	na	8.05 ± 6.34
GBC-SER PM	na	2.64 ± 0.46
GBC-QRT PM	na	9.89 ± 0.49
GBC-ARG-SLS PM	1.69 ± 0.14	29.84 ± 0.13

[a]na = Not applicable